Modified magnetic core-shell mesoporous silica nano-formulations with encapsulated quercetin exhibit anti-amyloid and antioxidant activity

Eleftherios Halevas [a], Barbara Mavroidi [a], Christiane M. Nday [e], Jianhua Tang [b], Graham C. Smith [b], Nikos Boukos [c], George Litsardakis [d], Maria Pelecanou [a], Athanasios Salifoglou [e]

[a] *Institute of Biosciences & Applications, NCSR "Demokritos", Athens 15310, Greece*

[b] *Faculty of Science and Engineering, University of Chester, Thornton Science Park, Chester CH2 4NU, UK*

[c] *Institute of Nanoscience and Nanotechnology, NCSR "Demokritos", Athens 15310, Greece*

[d] *Laboratory of Materials for Electrotechnics, Department of Electrical and Computer Engineering, Aristotle University of Thessaloniki, Thessaloniki 54124, Greece*

[e] *Laboratory of Inorganic Chemistry and Advanced Materials, Department of Chemical Engineering, Aristotle University of Thessaloniki, Thessaloniki 54124, Greece*

Abstract

Targeted tissue drug delivery is a challenge in contemporary nanotechnologically driven therapeutic approaches, with the interplay interactions between nanohost and encapsulated drug shaping the ultimate properties of transport, release and efficacy of the drug at its destination. Prompted by the need to pursue the synthesis of such hybrid systems, a family of modified magnetic core-shell mesoporous silica nano-formulations was synthesized with encapsulated quercetin, a natural flavonoid with proven bioactivity. The new nanocarriers were produced via the sol-gel process, using tetraethoxysilane as a precursor and bearing a magnetic core of surface-modified monodispersed magnetite colloidal superparamagnetic nanoparticles, subsequently surface-modified with polyethylene glycol 3000 (PEG3k). The arising nano-formulations were evaluated for their textural and structural properties, exhibiting enhanced solubility and stability in physiological media, as evidenced by the loading capacity, entrapment efficiency results and in vitro release studies of their load. Guided by the increased bioavailability of quercetin in its encapsulated form, further evaluation of the biological activity of the magnetic as well as non-magnetic core-shell nanoparticles, pertaining to their anti-amyloid and antioxidant potential, revealed interference with the aggregation of β-amyloid peptide (Aβ) in Alzheimer's disease, reduction of Aβ cellular toxicity and minimization of Aβ-induced Reactive Oxygen Species (ROS) generation. The data indicate that the biological properties of released quercetin are maintained in the presence of the host nanocarriers. Collectively, the findings suggest that the emerging hybrid nano-formulations can function as efficient nanocarriers of hydrophobic natural flavonoids in the development of multifunctional nanomaterials toward therapeutic applications.

Introduction

Applications of nanotechnology in biomedicine and pharmaceutics have provided an opportunity to address and treat challenging diseases by exploiting processes of drug encapsulation, biomolecular conjugation, and surface functionalization in the development of nanoparticle-based drug formulations [1]. Through manipulation of size and surface characteristics as well as diversity of starting materials used, emerging nanoparticles (NPs) can be developed into "smart vehicles", encasing therapeutic and imaging agents to improve their pharmacokinetic profile and bioavailability, thus facilitating targeted delivery and controlled release at the desired tissue, with minimum side effects [2]. Until today, several types of NPs have been used in biomedical applications as drug delivery systems [3–6], involving polymeric micelles, liposomes, dendrimers, block ionomer complexes, polymeric and inorganic particles, quantum rods and nanorods [7]. Compared to simple structure NPs, however, core-shell-structured NPs, exhibit a more diverse functional profile, mainly due to their unique structural characteristics and physicochemical properties, including reduced cytotoxicity, enhanced dispersibility, biocompatibility, increased chemical and thermal stability, and improved conjugation or surface modification with bioactive molecules [8].

One class of inorganic NPs with distinct advantages in drug delivery applications is mesoporous silica NPs (MSNPs) [9–11]. MSNPs possess a remarkably large surface area, well-defined pore arrangement with tunable pore sizes, adjustable design for the accommodation of drugs, imaging agents or both, and ease of inner and outer surface functionalization. These properties improve drug immobilization, stability in suspension, and sustained drug release [12]. MSNPs are chemically and thermally stable, however, their matrix undergoes biodegradation through hydrolysis. Degradation of MSNPs produces beneficial monomeric silicic acid [13], thus rendering MSNPs more appealing compared to other non-biodegradable species of inorganic NPs.

Magnetic targeting has been widely applied to direct MSNPs toward specific cellular targets and disease tissue locations [14]. This is commonly achieved through encapsulation of biocompatible superparamagnetic iron oxide (SPIO) NPs of proper surface architecture [15–19]. Key features of SPIOs include their ability to a) exhibit magnetization only in an applied magnetic field, b) form stable colloidal suspensions, especially in vivo, and c) direct themselves toward a specific site in the body by a magnetic force, thereby turning useful in controlled targeted drug delivery applications clinically. Furthermore, SPIO NPs possess uniform shape, controllable size distribution, strong magnetic susceptibility, and large surface area, which can be functionalized with specific biomolecules [20–22]. Research reports have proven that encapsulation of SPIO NPs in a mesoporous silica matrix enhances the chemical stability of magnetic NPs (MNPs) and reduces their potential cytotoxicity [23].

On the basis of the aforementioned, we herein report on the formation of core-shell magnetic mesoporous silica NPs (MMSNPs) as nanocarriers of the flavonoid quercetin (QC). QC (Fig. 1A) has received considerable attention due to its high radical scavenging activity and antioxidant potential [24–27]. Furthermore, QC plays an important neuroprotective role against agent-induced toxicity [28], and increases the resistance of neurons to excitotoxicity and oxidative stress by modulating mechanisms of cell death [29,30]. QC has been shown to protect primary neurons against the Aβ amyloid peptide in Alzheimer's disease, a property attributed to its antioxidant potential against the Aβ- induced oxidative stress [31] and also to its efficacy in preventing aggregation of Aβ into toxic assemblies (oligomers, protofibrils, amyloid fibrils) in vitro [32]. Its poor aqueous solubility and bioavailability, however, limits its therapeutic efficacy in clinical trials. As a result, several types of

nano-formulations have been presented for the efficient encapsulation of QC in an effort to overcome limitations arisen through its low bioavailability [33–41].

Aiming at the development of new multifunctional pharmaceutical nano-formulations involving antioxidant flavonoids, QC was encapsulated for the first time in modified magnetic core-shell MMSNPs. The anti-amyloidogenic and antioxidant activity of QC released from the MMSNPs was evaluated with biophysical studies involving circular dichroism (CD), thioflavin T fluorescence assay, and transmission electron microscopy, as well as biological assays in primary neuronal cell cultures. More specifically, a) the synthesis of polyethylene glycol 3000 (PEG3k) surface-modified monodispersed magnetite colloidal MNPs (Fe3O4-PEG3k NPs) was pursued, b) core-shell MMSNPs (mentioned henceforth as empty MMSNPs, EMMSNPs) were developed via the sol-gel method, c) the suitability of the arising core-shell MMSNPs, as potential nanocarriers of QC (mentioned henceforth as QC-loaded MMSNPs, QCMMSNPs), was evaluated, d) the structural and textural properties of the encapsulated material were investigated through

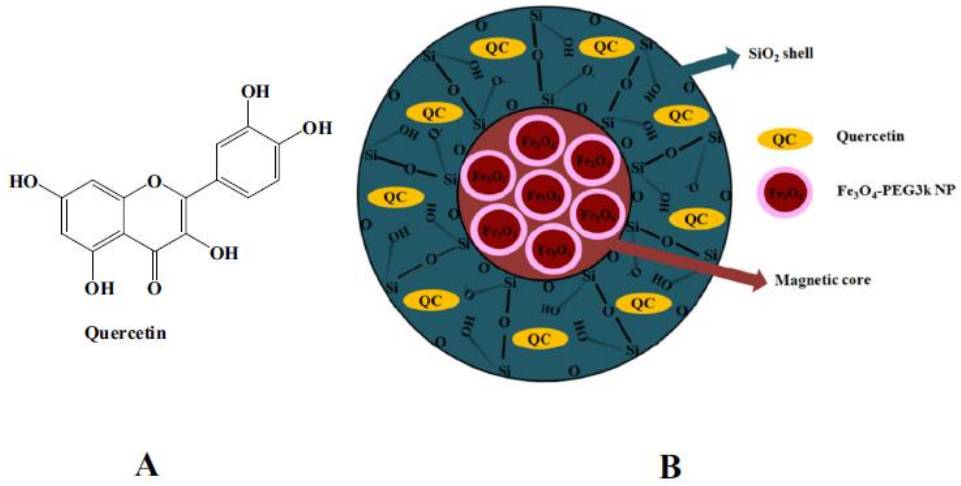

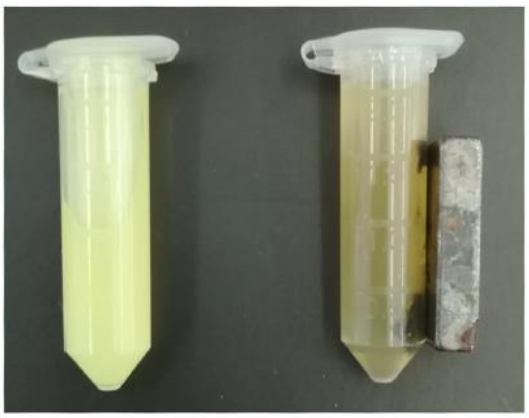

C

Fig. 1. A) Schematic representation of QC, **B)** Schematic illustration of a core-shell QCMMSNP, **C)** QC dispersed in PBS (left), QCMMSNPs dispersed in PBS (right). Encapsulation of QC in MMSNPs enhances its aqueous solubility

2. Experimental section

2.1. Materials

The starting materials used include: Iron(II) chloride tetrahydrate ($FeCl_2 \bullet 4H_2O$), iron(III) chloride hexahydrate ($FeCl_3 \bullet 6H_2O$), ammonia solution (~25%), polyethylene glycol 3000 monodisperse solution (PEG3k) (~50% in H_2O), quercetin (QC), tetraethyl orthosilicate (TEOS), and phosphate buffered saline (PBS) pH 7.4. All of the aforementioned materials were purchased from commercial sources (Sigma, Fluka) and were used without further purification. Ultrapure water (H_2O), methanol (MeOH), ethanol (EtOH) and dimethyl sulfoxide (DMSO) were used as solvents. Nitrogen gas was used for degassing ultrapure H_2O and establishment of nitrogen atmosphere during synthesis, where applicable. Amyloid peptide, Aβ40, was purchased from Anaspec (USA, >95% pure). The media/agents for the cultures of primary neuronal cells were purchased from Thermo Fisher Scientific (USA). The MTT reagent (3-[4,5-dimethylthiazol-2-yl]-2,5-diphenyl-tetrazolium bromide) was purchased from Applichem (Germany; >98% pure), while 2′ ,7′ -dichlorofluorescin diacetate (DCFH-DA) and thioflavin T (ThT) from Sigma-Aldrich (USA; >97% pure).

2.2. Characterization

FT-Infrared spectra were recorded on a Perkin Elmer 1760× FT-infrared spectrometer.

XRD data on Fe_3O_4-PEG3k NP, EMMSNP and QCMMSNP samples were acquired using a Bruker D8 Advance Eco diffractometer with Cu Kα radiation. Data were acquired with a 192-channel position sensitive detector at 0.01o intervals, using fixed divergence and detector slits, 2.5◦ anti-scatter Soller slits, and a Ni Kβ filter in the incident beam path. The samples were prepared for analysis by gentle grinding to a fine powder using a clean agate pestle and mortar. Subsamples were dispersed onto offset low-diffraction silicon sample mounts to generate uniform layers of approximately 0.5 mm in thickness.

Magnetization measurements on Fe_3O_4-PEG3k NP, EMMSNP and QCMMSNP dried powder samples were performed on a QD-Versalab Vibrating Sample Magnetometer (VSM), in fields up to 3 T and temperatures from 50 K to 400 K.

Transmission electron microscopy (TEM) images of Fe_3O_4 NPs, was acquired using a JEOL JEM-2100 Transmission Electron Microscope operated at 80 kV. 8 μL of the sample (PBS dispersion) was deposited onto a formvar/carbon coated grid for 2 min and subsequently stained with 2% wt•vol⍰ 1 uranyl acetate for 2 min. The sample was air-dried before TEM analysis. TEM images of Fe_3O_4-PEG3k NPs, EMMSNPs and QCMMSNPs were acquired using a FEI CM20 TEM, with particle size analysis performed manually through ImageJ software. Samples for TEM analysis were prepared by sonicating each one separately in heptane, and pipetting a portion of the resulting mixture onto a holey carbon support film on 300 mesh copper grid. The system was allowed to dry in air, leaving a small amount of each sample on the grid, ready for analysis. Images were obtained on a range of magnifications, using an accelerating voltage of 200 kV.

The morphology and detailed structural features of Fe_3O_4-PEG3k NPs, EMMSNPs and QCMMSNPs were investigated by scanning electron microscopy (SEM), using a high-resolution microscope FEI Quanta 3D FEG model, equipped with an energy dispersive X-ray (EDX) spectrometer Apollo X. Analyses were performed in high vacuum mode, at different accelerating voltages (5–20 kV), with the pellets being analyzed directly (samples were immobilized on a double-sided carbon tape, without coating).

Additional morphological and structural characteristics of the QCMMSNP samples were obtained via field emission scanning electron microscopy (FESEM), using a JSM-7000F microscope. A 10 μL sample (PBS dispersion, diluted 1:10) was deposited on a circular cover glass (immobilized on a double-sided carbon tape) and was air dried overnight. Samples were additionally covered with 10 nm Au/Pd sputtering. Data analyses were performed in high vacuum mode, in a 15 kV accelerating voltage.

XPS spectra of Fe3O4-PEG3k NPs, EMMSNPs and QCMMSNPs samples were acquired using a bespoke ultra-high vacuum system, fitted with a Specs GmbH Focus 500 monochromated Al Kα X-ray source and Specs GmbH Phoibos 150 mm mean radius hemispherical analyser with 9-channeltron detection. Survey spectra were acquired over the binding energy range 0–1100 eV, using a pass energy of 50 eV. High resolution scans over the C 1s, O 1s and Fe 2p photoelectron lines were made using a pass energy of 20 eV. Data were quantified using Scofield cross-sections, corrected for energy dependencies of the effective electron attenuation lengths and analyser transmission. Data processing and curve fitting were carried out using CasaXPS software v2.3.16. The samples were prepared for analysis by gentle grinding to a fine powder using a clean agate pestle and mortar.

Mean hydrodynamic diameter determination was pursued through Dynamic Light Scattering (DLS), using Photon Correlation Spectroscopy (Malvern S4700 PCS System, Malvern Instruments Ltd., Malvern, UK). Analysis was performed at a scattering angle of 90◦ and at 25 ◦C, using samples appropriately dispersed in PBS (pH 7.4). For each sample, the mean diameter ± standard deviation (±SD) of six determinations was calculated, applying multimodal analysis. Values reported are the mean diameter ± SD for three replicate samples.

Zeta-potential measurements on Fe3O4-PEG3k NP, EMMSNP and QCMMSNP samples were obtained through Laser Doppler Anemometry (Malvern Zetasizer IV, Malvern Instruments Ltd., Malvern, UK). All analyses were performed on samples, appropriately diluted with PBS buffer (pH 7.4), in order to maintain constant ionic strength. The refractive index and viscosity of the medium were set at 1.335 and 1.0200 [42], respectively. For each sample, the mean value standard deviation of four determinations was established. Values reported are the mean value SD of two replicate samples.

Discovery TGA 550 from TA Instruments was used to run the simultaneous Thermogravimetric Analysis (TGA) experiments. The instrument mass weighing resolution is 0.1 μg. A specific amount (mg) of each sample was placed in an open platinum sample pan for analysis. High purity air was used at a constant flow rate of 25 mL•min 1. During TGA analysis, the sample weight loss and rate of weight loss were recorded continuously under dynamic conditions, as a function of time or temperature, in the range from room temperature to 800 ◦C. Prior to activating the heating routine program, the entire system was purged with the appropriate gas for 10 min, at a rate of 25 mL•min^{-1}, to ensure that the desired environment had been established.

A Tristar 3000 Gas Adsorption Analyser and a VacPrep 061 Degasser by Micromeritics were used for the determination of the Brunauer- Emmett-Teller (BET) and Barrett-Joyner-Halenda (BJH) surface area, pore size and pore volume of the NPs via N2 gas sorption. The samples were properly weighed and degassed before installing them on the sample ports for analysis. About 150 mg of each sample was weighed on a balance and transferred to the sample tubes for degassing. Degassing was pursued by applying vacuum at room temperature for at least 48 h. After completion of sample degassing, analysis ensued.

Determination of entrapment efficiency and the in vitro release study of QC were performed through UV–Visible (UV–Vis) measurements on a Hitachi U-2001 spectrophotometer.

All measurements were performed immediately following NP preparation.

2.3. Synthesis of Fe3O4-PEG3k NPs

Quantities of 2.7 g (0.010 mol) of FeCl3·6H2O and 1.0 g (5.0 mmol) of FeCl2•4H2O were dissolved separately in two closed vessels in 20 mL of degassed ultrapure H2O, pretreated with inert nitrogen gas bubbling for 30 min, and then mixed in a three-neck flask under a nitrogen atmosphere. The resulting solution was vigorously stirred at 80 ◦C for 60 min. Subsequently, 6 mL of ammonia solution was added drop by drop until pH 10.5. The resulting mixture was allowed to stir for 30 min at 80 ◦C and then cooled to room temperature. A black precipitate was obtained from the reaction mixture via magnetic separation by means of a permanent magnet and the supernatant was removed by decantation. The resulting Fe3O4 NPs were washed three times with ultrapure H2O and resuspended in 20 mL of degassed ultrapure H2O in a three-neck flask under a nitrogen atmosphere. To that, 10 mL of PEG3k solution was added under vigorous stirring and the resulting mixture was further stirred for 60 min at 50 ◦C. Subsequently, ammonia solution was added until pH 7.5 under continuous stirring and the mixture was allowed to stir for an additional 2 h at 50 ◦C. A dark brown precipitate was collected by centrifugation at 6000 rpm for 30 min at 25 ◦C. The resulting Fe3O4-PEG3k NPs were washed three times, with ultrapure H2O, to remove unreacted PEG, recentrifuged and resuspended in 20 mL of degassed ultrapure H2O in a closed dark vessel, and stored at 4 ◦C for further use. Unmodified Fe3O4 NPs, without PEG3k stabilization, were prepared for comparative purposes in the ensuing physicochemical characterization and biological experiments, following a similar procedure with no addition of PEG3k.

2.4. Synthesis of QCMMSNPs

A quantity of 0.25 g of dried Fe3O4-PEG3k NPs at 50 ◦C for 24 h was suspended in 20 mL of degassed ultrapure H2O in a three-neck flask under a nitrogen atmosphere. Subsequently, ammonia solution was added until pH 8.0 under continuous stirring and the mixture was allowed to stir for an additional 10 min at 50 ◦C. Then, 0.25 g of QC and 40 mL of ethanol were mixed at 50 ◦C, under continuous stirring, and added to the suspension. The resulting mixture was further stirred vigorously for 80 min at 50 ◦C. To the mixture, 7 mL of TEOS was dripped in, and the resulting solution was vigorously stirred for 18 h at 50 ◦C. On the following day, a dark brown-green precipitate was obtained after centrifugation of the reaction mixture at 6000 rpm for 30 min at 25 ◦C, rinsed three times with ultrapure water to remove non-encapsulated QC, recentrifuged, and stored at 4 ◦C in a closed dark vessel for further use. EMMSNPs were synthesized following the same procedure with no addition of QC.

2.5. Synthesis of EMSNPs and QCMSNPs

EMSNPs and QCMSNPs, with 0.25 g of QC, as the initial amount of flavonoid employed in the encapsulation procedure, were synthesized according to previously reported work [37]. They were used for comparative purposes in the ensuing biological experiments.

2.6. Determination of QC entrapment efficiency and loading capacity

The percentage of encapsulated QC into QCMMSNPs was estimated by UV–Visible spectrophotometry at the characteristic wavelength of QC absorption (370 nm) [43]. A quantity of 0.10 g of QCMMSNP powder was ground and immersed into 30 mL of MeOH-DMSO solution (MeOH: DMSO, 5:1 *v*/v). The resulting QCMMSNP dispersion was sonicated for 20 min and vortexed for 10 min, in order to ensure complete release of the encapsulated QC. The resulting empty precipitated MMSNPs were removed by centrifugation at 6000 rpm for 25 min at 25 ◦C. An aliquot of 3 mL was withdrawn with a pipette and the absorbance of the supernatant clear solution was measured following appropriate dilutions. The concentration of QC was determined using the following

calibration curve of QC concentrations in MeOH-DMSO solution vs. absorbance values: A = 77.32C + 0.025 (R2 = 0.997), where A is the absorbance at 370 nm and C is the concentration of QC ($mg \bullet mL^{-1}$). The entrapment efficiency and loading capacity of QC were calculated using the following equations:

Entrapment Efficiency (%) = QCi/QCt × 100, where QCi is the amount (mg) of QC incorporated into MSNPs and QCt is the initially added amount of QC, respectively.

Loading Capacity (%) = QCi/WQCMMSNPs × 100, where QCi is the amount of QC (mg) incorporated into QCMMSNPs and WQCMMSNPs is the weight of the synthesized QCMMSNPs after drying. Experiments were carried out in triplicates and the results were expressed as mean ± SD.

2.7. In vitro QC release study

The QC release profile of QCMMSNPs was obtained as follows: 0.10 g of QCMMSNP powder was ground and immersed into 30 mL of PBS (pH 7.4), under continuous stirring at a rate of ca. 400 rpm, at 37 ± 1 ◦C. Aliquots of 3 mL were withdrawn with a syringe, at fixed time intervals, for analysis and centrifuged at 6000 rpm for 1 min, to remove the insoluble QCMMSNP residue. The amount of QC released was determined by UV–Vis spectrophotometry in the clear solution at 370 nm via the aforementioned calibration curve (vide supra). Experiments were carried out in triplicates and the results were expressed as mean ± SD.

2.8. Preparation of Aß and NP samples

Aβ40 was gently dissolved without vortexing in Type 1 (Milli-Q) water to a final concentration of 100 μM. Solutions of plain Aβ40 in phosphate buffer (PB, 10 mM, pH 7.33) were prepared by adding PB to aliquots of the 100 μM stock to achieve final concentration of 50 μM. In the preparation of the Aβ/NP mixtures, the ratios 1:0.5 and 1:1 were calculated based on the amount of QC released from each kind of NP, as projected into their respective release curves (Section 3.12) [37]. Based on the curve, the proper amount (mg) of NPs was weighed in order to prepare a 100 μM solution of released QC in PB. To prepare the Aβ:NP 1:1 ratio, equal volumes of the 100 μM Aβ stock and the 100 μM QC solution were mixed. For the Aβ:NP 1:0.5 ratio, a dilution in half of the 100 μM QC solution with PB was necessary. Verification of the amount of QC present in solution was made through UV–Vis measurements (Section 3.13) of the samples.

2.9. Circular dichroism studies

Appropriate amounts of well-dried NPs were weighed and added to 50 μM Aβ40 solutions to give the desired Aβ:NP molar ratios of 1:0.5 and 1:1. Aβ structural changes were monitored for approximately 30 days at 33 ◦C under quiescent conditions. CD spectra were recorded on a JASCO J-715 spectropolarimeter (Jasco Co., Japan) in the range of 190–260 nm, with a 1 mm path length quartz cuvette. Each spectrum was the average of three scans at a rate of 100 nm·min 1 and a resolution of 0.5 nm. Three independent experiments were performed for each condition and in each case solutions of plain Aβ, NPs and QC were run as controls. Analysis of the CD data was performed using the OriginPro 9 program. In the absence of Aβ, the NPs, being investigated, exhibit weak CD signals that do not change with time (Fig. S3, Supplementary Information).

2.10. Thioflavin T assay

For the ThT assay, 100 μL of the aged (30 days) CD solutions of Aβ40 (with or without the NPs) was diluted to half with PB (10 mM, pH 7.33), to obtain 200 μL of final solutions with theoretical Aβ40 concentration of 25 μM. To these solutions, a stock solution of ThT in PBS (10 mM, pH 7.33) was added to achieve a final concentration of ThT of 5 μM. The mixture was well-agitated by pipetting

and immediately thereafter fluorescence was monitored following excitation at 440 nm (emission slit = 2.5 nm, PMT Voltage 700 V, response 0.4 s) with a HITACHI F- 2500 spectrofluorimeter. The analysis of fluorescence data was performed using the OriginPro 9 program.

2.11. Cell cultures

Hippocampal neuronal cultures were obtained from postnatal mice (<2 day old). Briefly, after being dissected, the hippocampus was incubated with 0.25% trypsin for 15 min at 37 ◦C. The hippocampi were then rinsed in 10 ml of Hibernate, containing 10% (*v*/v) heat-inactivated fetal bovine serum (FBS). Cultures were maintained in Neurobasal-A medium containing 2% B-27 supplement, 0.5 mM Gluta-MAX and 1% penicillin/streptomycin at 37 ◦C and 5% CO2. Half of the medium was replaced twice a week. For MTT cytotoxicity and Reactive Oxygen Species (ROS) intracellular studies, neuronal hippocampal cells were plated at a density of approximately 2 × 104 per well in 96-well plates and incubated at 37 ◦C for 24 h to allow cells to attach, followed by seven additional days of incubation to allow cells to differentiate. For all measurements, cells were subsequently treated with the indicated concentrations of Aβ in the presence or absence of NPs, as described in the next paragraph.

2.12. Cell viability evaluation

Solutions of Aβ40 (10 μM) in PBS, in the absence or presence of NPs (1:1 and 1:2 ratio of Aβ:NPs, based on the released QC (Section 3.13)), pre-incubated at 37 ◦C, were diluted with fresh medium and added to individual wells at a final concentration of Aβ40 of 1 μM. According to our previous studies [44], pre-incubation of Aβ40 for 3 d was necessary in order for Aβ40 to exert maximum neurotoxicity. After a 24 h exposure of cells to the Aβ40 solutions, 100 μL of a 0.5 mg•mL⍰ 1 stock solution of MTT in Neurobasal-A was added to each well of primary hippocampal neurons, followed by a 3 h incubation at 37 ◦C. The medium was removed and the cells were diluted in DMSO. The relative formazan concentration was measured by determination of the absorbance at 540 nm (Tecan well plate reader). Results were expressed as percentage of MTT reduction, assuming that the absorbance of control (untreated) cells was 100%. Data are presented as the mean of three independent experiments with six replicate wells for each condition. Graphs were analyzed using GraphPad Prism 5.0 software. In each run, the effect of solutions of plain Aβ and NPs was independently checked to serve as internal standard.

2.13. Intracellular ROS measurements

Primary hippocampal neurons were treated with Aβ40 and NP solutions as previously described in Section 2.12. After incubation for 24 h, cells were washed with PBS and incubated with 10 μM of DCFH-DA for 30 min at 37 ◦C in the incubator with 5% CO2. The fluorescence intensity of DCF, representing ROS levels, was determined using a Tecan fluorescence well plate reader, at the excitation wavelength of 485 nm and emission wavelength of 528 nm. Control groups consisted of cells incubated with medium only and plain Aβ or NPs.

2.14. Statistical analysis

Data in all assays are the mean of at least three independent experiments. The statistical significance of changes in different groups was evaluated by one-way analysis of variance (ANOVA) and Student *t*-tests, using GraphPad Prism 5.0 software. For each experiment, data are expressed as the mean ± standard error of the mean (SEM, $n = 3$), $*p \leq 0.05$, $**p \leq 0.01$, $***p \leq 0.001$, ns (not significant) > 0.05.

3. Results and discussion

3.1. Synthesis

modified Massart method was used for the synthesis of Fe3O4 NPs, which were employed as the main core of the nanocarriers. More specifically, ferric chloride and ferrous chloride in a 2:1 molar ratio were co-precipitated upon addition of excess ammonia solution [45,46]. The surface of the obtained Fe3O4 NPs was negatively charged through surface functionalization with PEG3k, in order to generate a ferromagnetic suspension of colloidal, structurally stabilized, Fe3O4 NPs, surface-modified with long polymeric PEG chains (Scheme 1). In general, surface functionalization of superparamagnetic magnetite NPs with biocompatible polymeric moieties, such as PEG, reduces their cytotoxicity, improves their colloidal stability in physiological media by preventing agglomeration, and enhances their blood circulation half-life (Scheme 1) [47]. Both procedures, co-precipitation and surface modification with PEG3k, were carried out under anaerobic conditions and vigorous stirring at constant temperature, 80 ◦C, and 50 ◦C, respectively, to ensure reagent homogeneity, and in the liquid phase to prevent surface passivation of the produced NPs. The high pH (pH 10.5), maintained during the Fe3O4 NP synthetic procedure, prevented surface charge-induced agglomeration, since the isoelectric point of Fe3O4 depends highly on pH (6.25 ≤ pH ≤ 7.10) [48–51], temperature, and Fe(II) concentration [52,53]. During surface modification with PEG3k, the pH of the reaction was 7.5, in order to ensure: i) negative particle surface charge of the resulting PEGylated MNPs [54], ii) stabilization of the NP size by both electrostatic and steric repulsion between PEG chains on the surface of the particles [55], and iii) enhanced NP stability in aqueous media, at pH in the near-physiological pH range [56]. Core-shell QCMMSNPs (Fig. 1B) were prepared following initial incorporation of an ethanolic solution of QC to an aqueous dispersion of Fe3O4-PEG3k NPs and subsequent formation of SiO2 nanocarriers via sol-gel reaction upon addition of tetraethoxysilane (TEOS) to the emerging flavonoid- MNPs mixture. Ammonia was employed as the catalyst of TEOS hydrolysis, in order to achieve better control of size and morphology of the resulting silica powders [57]. The employed sol–gel process describes the transition of a system from a sol, a liquid with relatively low viscosity, into a solid gel phase through condensation and cross-linking of the emerging colloidal particles, resulting in an intense enhancement of viscosity [58]. A silicon alkoxide, such as TEOS, is used as the precursor for the sol–gel reaction. At first, a hydrolysis reaction of the alkoxide takes place, which is catalyzed by a base or an acid (Scheme 2). Hydrolysis products include hydrated silica tetrahedra that interact further via a condensation reaction to give rise to intermediate moieties linked through a siloxane bond [Si-O-Si] (Scheme 2). Further polycondensation leads to formation of a silica network (Scheme 2) through linkage of additional silanols. The condensation products are water and alcohol, which remain in the pores of the silica network [58]. The effective encapsulation of QC into the MMSNPs aims at improving its aqueous solubility, circulation time, systemic bioavailability, targeted delivery, controlled release, thus contributing to enhanced therapeutic potential. Indeed, as can be seen in Fig. 1C, encapsulation of QC efficiently enhances its solubility in aqueous media (PBS).

3.2. FT-IR spectroscopy

The FT-IR spectra of Fe3O4 NPs, PEG3k, and Fe3O4-PEG3k NPs are presented in Fig. 2A. More specifically, the spectrum of unmodified Fe3O4 NPs shows two characteristic absorption bands attributed to the Fe □ O vibrations, a weak shoulder at 620 cm□ 1 and a sharp band at 537 cm□ 1 [59]. Similar absorption bands have been observed in the spectrum of Fe3O4-PEG3k NPs at 623 cm□ 1 and at 548 cm□ 1 [60]. In the spectrum of PEG3k, the broad absorption band observed at around 3448 cm□ 1 can be attributed to the O □ H stretching vibrations, whereas the sharp absorption bands at 2916 cm□ 1 and 1103 cm□ 1 can be assigned to the C □ H and C □ O stretching vibrations,

respectively [48]. Similar absorption bands have been observed in the spectrum of Fe3O4-PEG3k NPs at 3430 cm 1 for the O H stretching vibrations, 2988 cm 1 for the C H stretching vibrations, and 1066 cm 1 for the C O stretching vibrations, respectively. The above results indicate successful surface modification of Fe3O4 NPs with PEG3k.

The FT-IR spectra of EMMSNPs, QC, and QCMMSNPs are presented in Fig. 2B. More specifically, in the spectrum of EMMSNPs, characteristic absorption bands assigned to the Fe O vibrations are observed at 621 cm 1 and 556 cm 1. The very broad absorption band at around 3359 cm 1, the broad plateau observed at around 2955 cm 1, and the sharp absorption band at 1070 cm 1 can be attributed to the O H, C H, and C O stretching vibrations, respectively, of the PEG3k moieties on the surface of the encapsulated Fe3O4-PEG3k NPs. The Si–O–Si symmetric stretching and bending vibrations appear at 766 cm 1 and 479 cm 1, respectively, with Si–O–Si antisymmetric stretching vibrations appearing at 961 cm 1 [61,62]. In the spectrum of QCMMSNPs, the absorption bands attributed to the O H, C H, and C O stretching vibrations of the PEG3k moieties of the encapsulated PEGylated MNPs are observed at 3204 cm 1, 2876 cm 1, and 1061 cm 1, respectively. The Fe O vibrations are observed at 620 cm 1 and 550 cm 1. The Si–O–Si symmetric stretching and bending vibrations are observed at 798 cm 1 and 470 cm 1, respectively, with Si–O–Si antisymmetric stretching vibrations appearing at 948 cm 1. The characteristic carbonyl (–C=O) and aromatic stretching vibrations of QC are observed at 1652 cm 1 and 1598 cm 1, respectively, with phenolic O–H bending vibrations observed around 1319 cm 1 and 1350 cm 1 [63,64]. The obtained results confirm a successful encapsulation of QC in the MMSNPs.

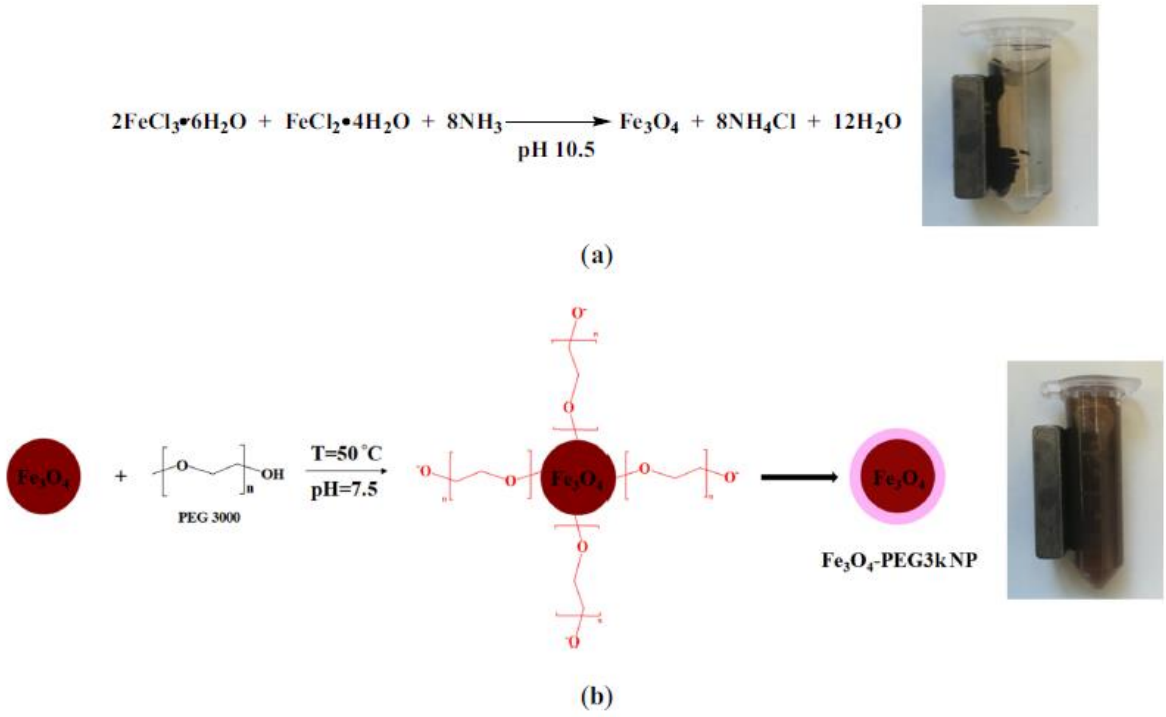

Scheme 1. a) Chemical reactivity showing the synthesis of Fe3O4 NPs, and **b)** Schematic illustration of NP further functionalization to a colloidal suspension of Fe3O4-PEG3k NPs.

3.3. X-ray diffraction

Data from 9◦ to 95◦ for the Fe3O4-PEG3k NP, EMMSNP, and QCMMSNP samples are shown in Fig. 3. The three traces are offset vertically for clarity. The main diffraction peaks for Fe3O4 (magnetite), with their Miller indices, are labelled using reference data from the JCPDS PDF database card

reference 01–086-1339 (star quality). In the case of the QCMMSNP sample, additional low intensity peaks were detected in the lower angle range and are matched with reference data for QC (PDF reference 00–043-1695). The broad hump in the data peaking at approximately 21◦–22◦, seen for EMMSNP and QCMMSNP samples, is attributed to amorphous silica. The background intensity, particularly noticeable in the case of the Fe3O4-PEG3k NP sample, is due to fluorescence from the Fe-containing sample material. The origin of the broad structure in the range ~ 10◦–15◦ is unknown. However, it corresponds to spacings in the range of ~0.3–0.44 nm, indicating a weaker structure on this scale. Low angle data (2o < 2θ < 10o) on QCMMSNP samples suggest no ordered pore structure.

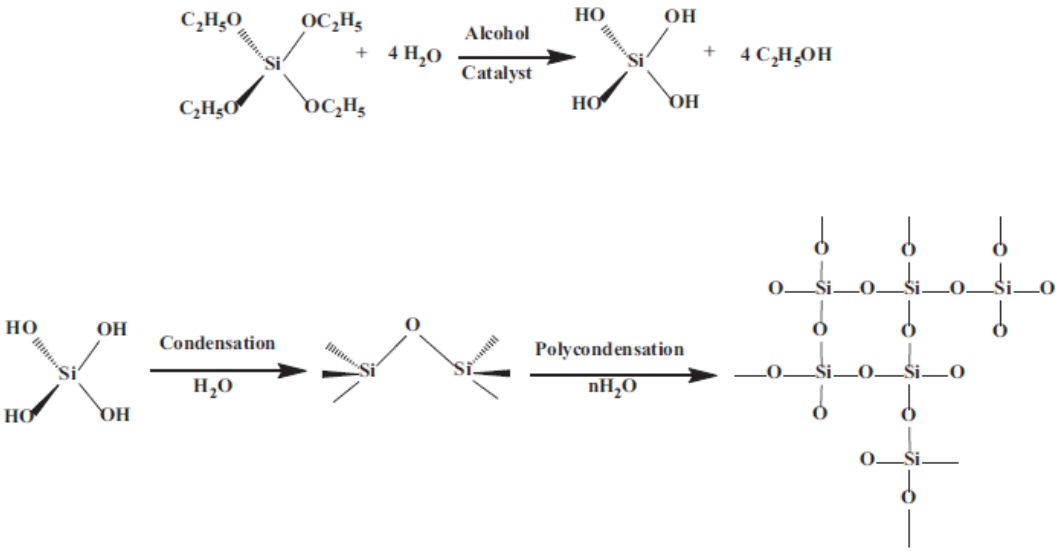

Scheme 2. Simplified illustration of TEOS condensation in a sol-gel process.

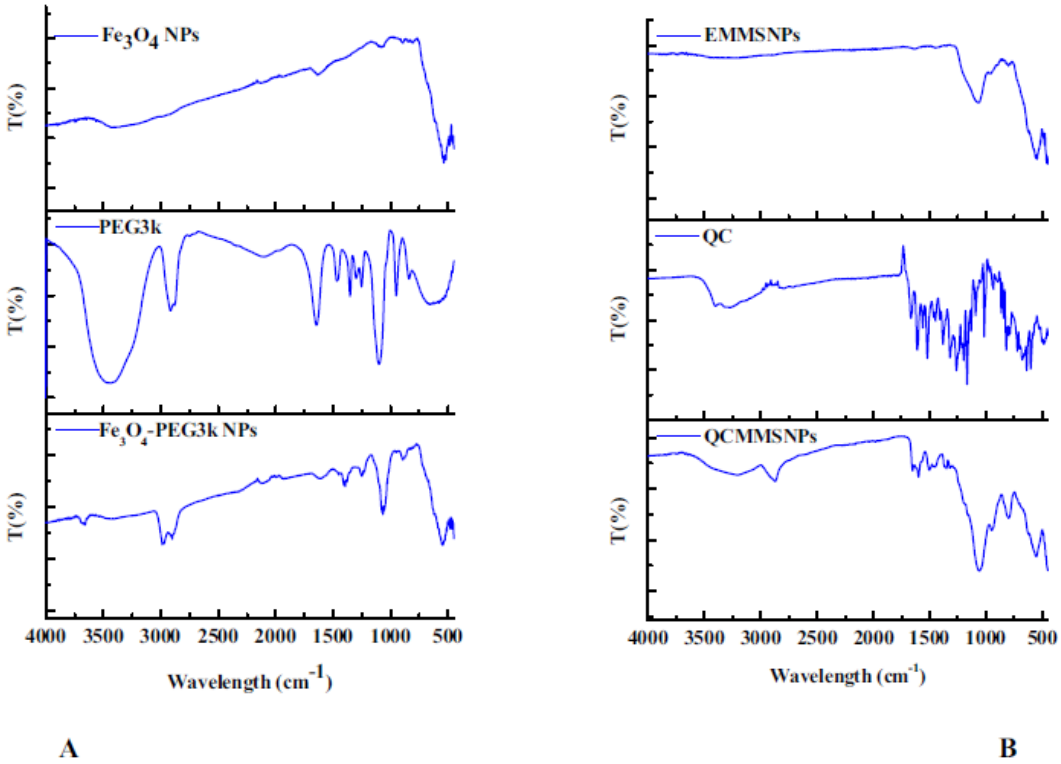

Fig. 2. FT-IR spectra of **A)** Fe3O4 NPs, PEG3k, and Fe3O4-PEG3k NPs, and **B)** EMMSNPs, QC, and QCMMSNPs

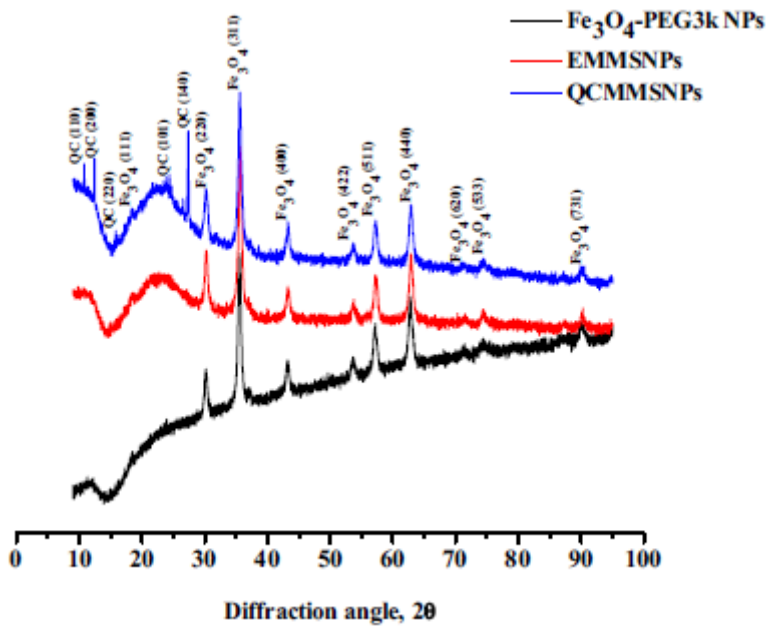

Fig. 3. XRD data from Fe3O4-PEG3k NP, EMMSNP, and QCMMSNP samples, offset vertically for clarity and with principal diffraction peaks labelled.

3.4. XPS measurements

3.4.1. XPS composition analysis

XPS analysis of the Fe3O4-PEG3k NP samples showed the presence of only Fe, O and C. In addition, Si was detected in EMMSNP and QCMMSNP samples. The survey spectra are shown in Fig. 4I, with the principal peaks labelled. The data were quantified to provide the surface composition shown in Table 1. It should be noted that the method of quantification a) provides an average composition in atom % over the information depth of the technique, assuming that composition does not vary within this depth, and b) is weighted toward the outermost surface layers. The information depth is in the range of ~5–10 nm, depending on sample composition and photoelectron energy. H and He are not detected by XPS. In the case of the Fe3O4-PEG3k NP sample, the ratio of Fe to O in Table 1 is not correct for Fe3O4. However, the sample is treated with PEG3k, which presumably coats the surface of the Fe3O4 NPs, in which case the Fe 2p signal would preferentially be attenuated by the carbon-containing overlayer relative to the O 1 s, thereby accounting for the apparent discrepancy. A similar argument applies to the apparent ratio of O to Si in the EMMSNP and QCMMSNP samples.

3.4.2. XPS chemical state analysis

Scans were run over individual photoelectron lines to provide additional information on the chemical states of the elements present (Figs. 4II–V). The Fe 2p spectrum for the Fe3O4-PEG3k NP sample consisted of a doublet due to the Fe 2p3/2 and 2p1/2 components, at approximately 710–711 eV and 719–720 eV binding energy, respectively. Each of these components is accompanied by a shake-up peak, approximately 13 eV higher in binding energy. In the case of the Fe3O4- PEG3k NP sample, each main doublet component was fitted with two contributions to intensity, representing Fe(II) and Fe(III) in the Fe3O4 structure, which may be expressed as FeO•Fe2O3. The fitted components and constraints used during fitting are summarized in Table 2, confirming the Fe present as Fe3O4. This peak fitting model was applied to the Fe 2p XPS data from the EMMSNP and QCMMSNP samples and produced satisfactory fits, showing that the oxidations state of the Fe had

not changed during subsequent treatments. However, it should be noted that the peak fitting for the EMMSNP sample and especially for the QCMMSNP sample was rather complex, mainly due to the rather poor signal to noise ratios, which can be attributed to the low levels of Fe present in these samples.

The curve-fitted O 1s peaks are shown in Fig. 4III. The O 1s from the Fe3O4-PEG3k NP sample was fitted with three components at approximately 530.1 eV, 531.3 eV, and 532.8 eV. The component at 532.8 eV is in very good agreement with reference data for PEG3k. The component at 530.1 eV is in good agreement with reference data for Fe3O4. It was not possible to obtain a satisfactory fit to the O 1s data from this sample, using just these two components. The additional component at 531.3 eV was attributed to the modification of the Fe3O4 surface states due to the presence of PEG3k. The O 1s lines from the EMMSNP and QCMMSNP samples are dominated by strong components at 532.9–533.1 eV, due to oxygen bonded to Si in the amorphous SiO2 phase. In both cases, weak contributions to intensity at approximately 530.3 eV can be seen, due to the low level of Fe3O4 detected. At these levels, the possible Fe3O4/ PEG3k surface interaction component was not detected.

The Si 2p peaks from the EMMSNP and QCMMSNP samples are shown in Fig. 4IV. In both cases, they are fitted by a single component at approximately 103.6 eV binding energy, consistent with Si in a SiO2 formulation.

Curve-fitted C 1s spectra are shown in Fig. 4V. The spectrum from the Fe3O4-PEG3k NP sample showed a main component at 286.5 eV, in agreement with reference data for ester bonds as in PEG3k. In addition, a weak component at approximately 288.6 eV was detected. This is indicative of a carbon in a more polar oxygenated environment and may be associated with the 531.3 eV component in the O 1s spectrum of this sample and attributed to the Fe3O4/PEG3k interactions. The spectrum of the EMMSNP sample is similar to that of the Fe3O4-PEG3k NP sample, with an additional low-level component at a lower binding energy, typically associated with carbon in C–C hydrocarbon bonds. This may indicate a low level of additional material introduced with the SiO2 NPs. The spectrum from the QCMMSNP sample showed a strong component at approximately 285.0 eV, a relatively strong component at approximately 286.7 eV and a weaker component at approximately 289.2 eV. The 285.0 eV component is attributed to carbon atoms bonded to adjacent carbons in the QC molecular structure. The component at 286.7 eV is attributed to carbon singly-bonded to oxygen in either the hydroxyl groups or the γ-pyrone fragment of QC, and also to the C-O-C bonds in PEG3k. The weaker component at 289.2 eV may arise from the carbonyl bond in QC, but this also overlaps with the component at approximately 288.6 eV detected in the Fe3O4-PEG3k and EMMSNP samples, prepared without QC and attributed to the Fe3O4-PEG3k interactions.

Table 1
XPS Surface composition of Fe_3O_4-PEG3k NP, EMMSNP and QCMMSNP samples, in atom %.

Atom	Sample		
	Fe_3O_4-PEG3k NPs	EMMSNPs	QCMMSNPs
C 1 s	25.0	15.8	31.8
O 1 s	54.4	54.1	42.7
Si 2p		28.4	25.2
Fe 2p	20.6	1.7	0.4

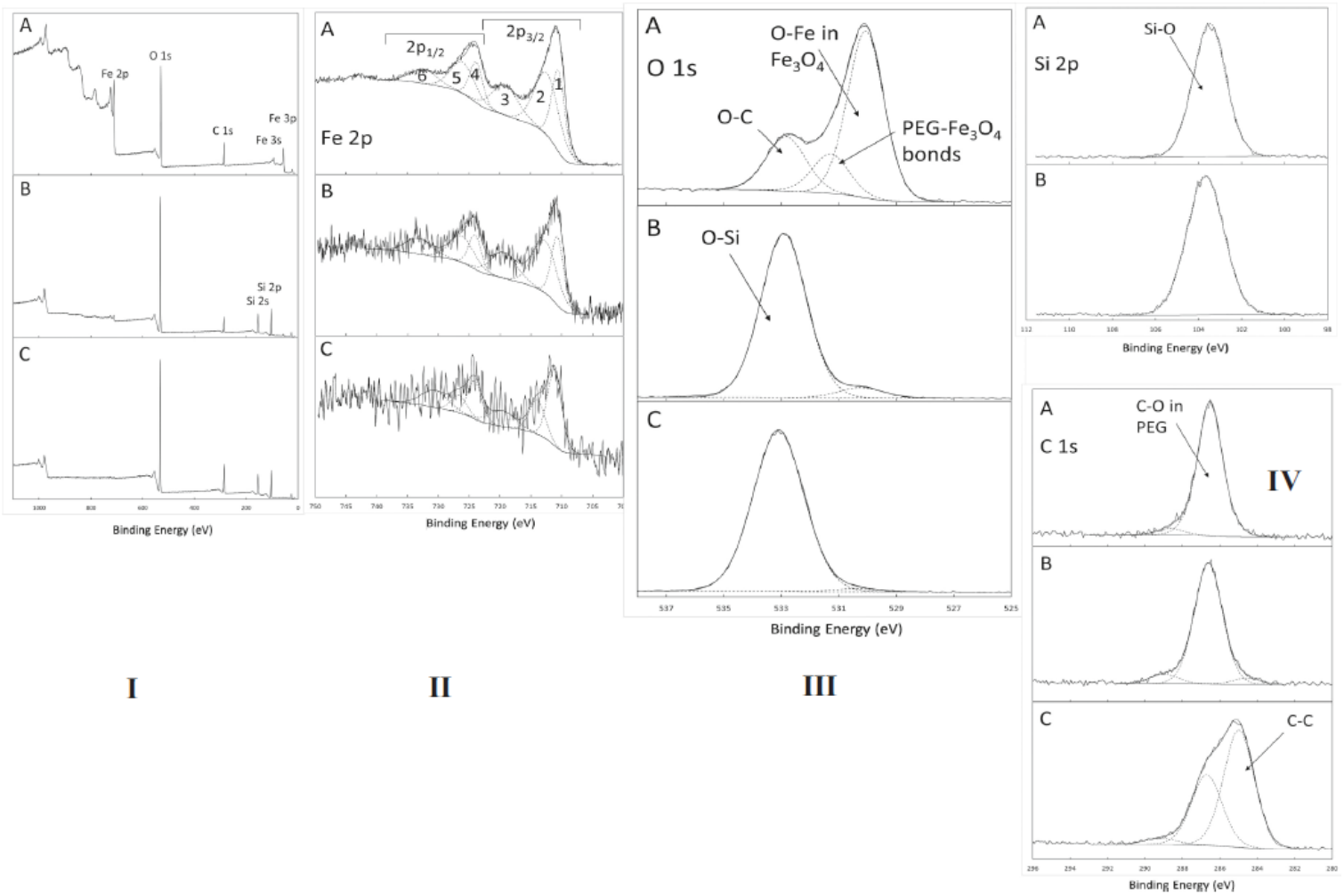

Fig. 4. I. XPS survey spectrum with principal photoelectron peaks labelled for **A)** Fe3O4-PEG3k NPs, **B)** EMMSNPs, and **C)** QCMMSNPs. **II.** Curve-fitted Fe 2p spectra for **A)** Fe3O4-PEG3k NPs, **B)** EMMSNPs, and **C)** QCMMSNPs. The fitted components, numbered 1 through 6, are as described in Table 2. **III.** Curve-fitted O 1 s spectra for **A)** Fe3O4-PEG3k NPs, **B)** EMMSNPs, and **C)** QCMMSNPs. **IV.** Curve-fitted Si 2p spectra for **A)** EMMSNPs and **B)** QCMMSNPs. **V.** Curve fitted C 1 s spectra for **A)** Fe3O4-PEG3k NPs, **B)** EMMSNPs, and **C)** QCMMSNPs.

Table 2
Peak fit parameters from Fig. 4.

Peak number	Line	Oxidation state	Position (eV)	(FWHM) (eV)	% of intensity	Fitting constraint
1	Fe $2p_{3/2}$	Fe^{2+}	710.52	2.49	20.66	
2	Fe $2p_{3/2}$	Fe^{3+}	712.36	4.64	30.51	
3	Shake-up		719.15	5	15.52	
4	Fe $2p_{1/2}$	Fe^{2+}	723.84	2.49	10.34	Equal FWHM and 50% intensity of peak 1
5	Fe $2p_{1/2}$	Fe^{3+}	726.02	4.64	15.49	Equal FWHM and 50% intensity of peak 2
6	Shake-up		732.37	5	7.75	Equal FWHM and 50% intensity of peak 3

3.5. TEM analysis

TEM images of air-dried Fe3O4 NPs, FE3O4-PEG3k NPs, EMMSNPs, and QCMMSNPs are presented in Figs. 5A–G. TEM observations of Fe3O4 NPs (Fig. 5A) indicate their spherical morphology, with their average particle size being between 6 and 9 nm. TEM images of Fe3O4-PEG3k NPs (Figs. 5B and C and S2A, Supplementary Information) indicate the presence of predominantly spherical PEGylated magnetite NPs, with an average particle size between 20 and 30 nm and scattered small Fe3O4 aggregates surrounded by a PEG3k layer. This aggregation could be attributed to the strong magnetic attraction between magnetite NPs, the repeated centrifugations during the synthetic procedure, the magnetic agitation during the stabilization with PEG3k, and the drying process before TEM measurements [66]. TEM images of the EMMSNP sample (Fig. 5D and E) project the presence of relatively globular core-shell magnetic silica nano-formulations around 120–140 nm with encapsulated distinct and agglomerated Fe3O4-PEG3k NPs formulating the magnetic core. In the case of the QCMMSNP sample (Fig. 5F and G), TEM observations suggest the presence of relatively agglomerated core-shell magnetic silica nanospheres, with sizes in the range 200–250 nm. The observed difference between the particle sizes of the empty and QC-loaded samples could be attributed to the presence of QC in the pores of the nanospheres that induces swelling of the silica matrix and thus an increase in the diameter of the produced QCMMSNPs.

3.6. SEM and FESEM analysis

The morphologies of all prepared samples were examined by SEM. Fig. 6 presents SEM images of the morphology of Fe3O4-PEG3k NPs (Fig. 6A), EMMSNPs (Fig. 6B), and QCMMSNPs (Fig. 6C), respectively. All samples display large and dense agglomerates of aggregated NPs, with an approximately uniform spherical morphology and a relatively narrow size distribution. In addition, FESEM examination of the QCMMSNP sample (Figs. S2B and S2C, Supplementary Information) further confirmed the presence of distinct core-shell nanospheres with sizes ranging between 200 and 250 nm.

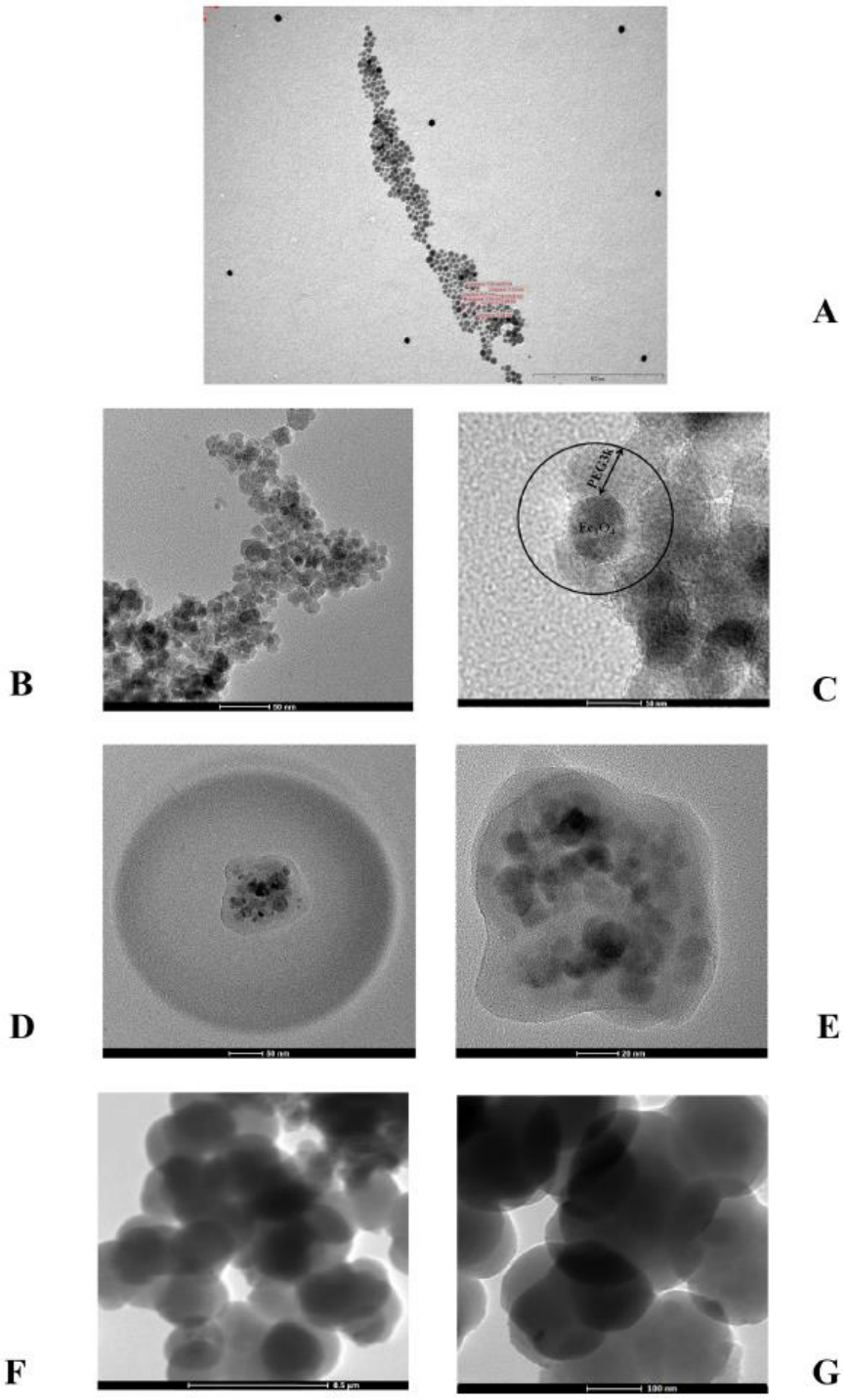

Fig. 5. TEM images of **A)** Fe3O4 NPs at 0.2 µm, **B)** Fe3O4-PEG3k NPs at 50 nm, and **C)** 10 nm, **D)** EMMSNPs at 50 nm, and **E)** 20 nm, **F)** QCMMSNPs at 0.5 µm, and **G)** 100 nm.

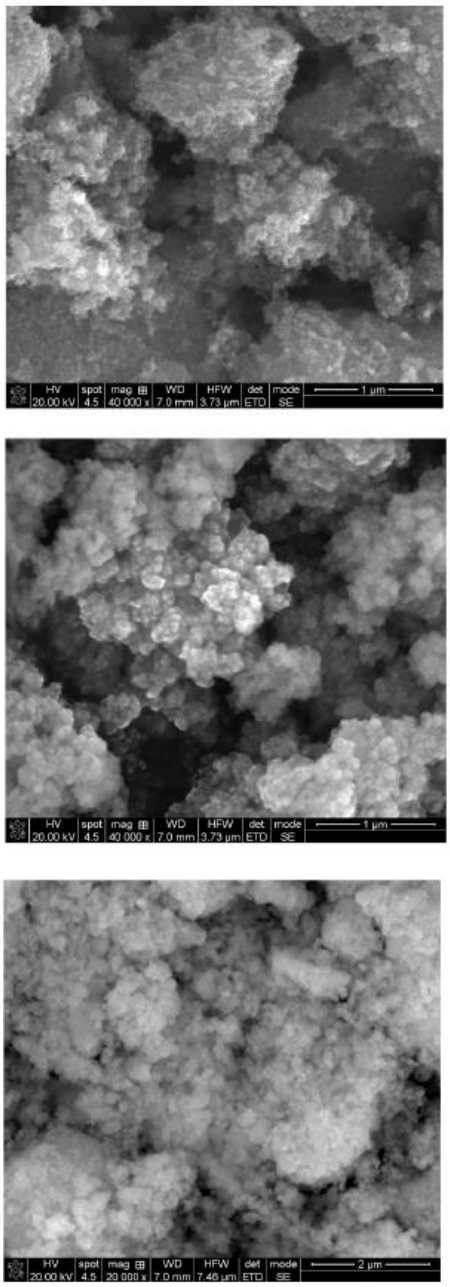

Fig. 6. SEM images of A) Fe_3O_4-PEG3k NPs at 1 µm, B) EMMSNPs at 1 µm, and C) QCMMSNPs at 2 µm.

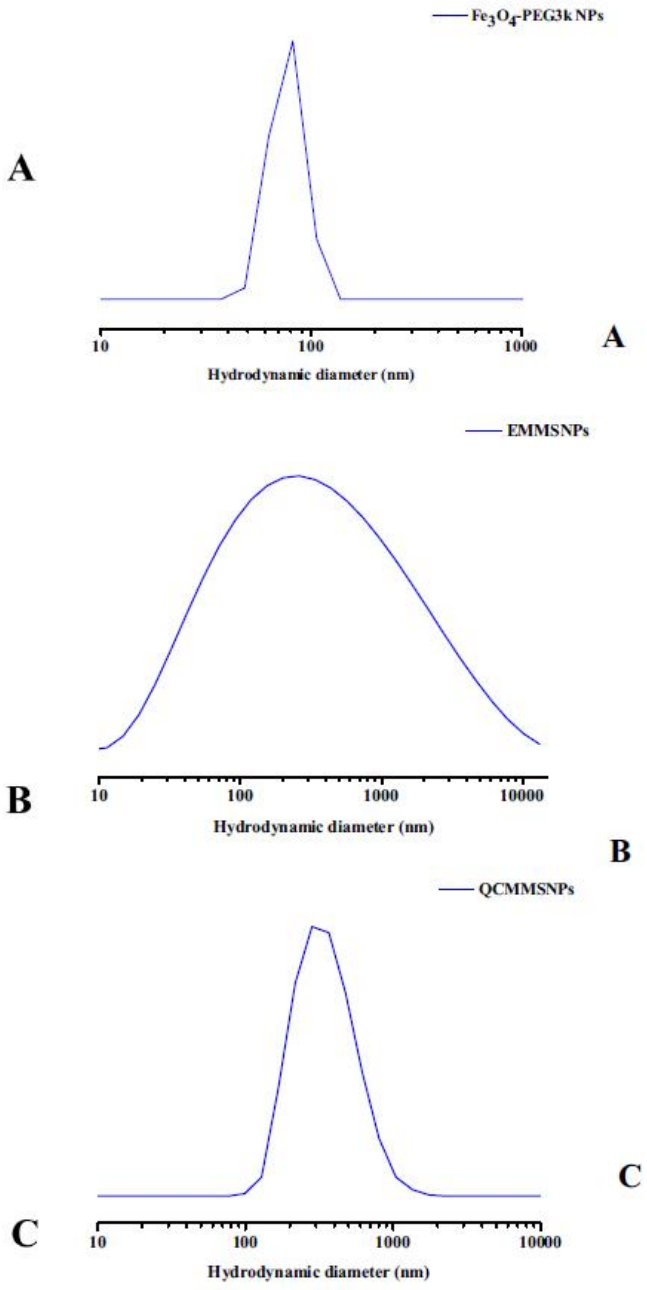

Fig. 7. Particle size distribution of A) Fe_3O_4-PEG3k NPs, B) EMMSNPs, and C) QCMMSNPs.

3.7. DLS and z-potential

of appropriately diluted, with PBS buffer (pH 7.4), Fe3O4-PEG3k NP, EMMSNP and QCMMSNP samples, as presented in Figs. 7A–C. The results obtained indicate that the mean hydrodynamic diameter of Fe3O4- PEG3k NPs is around 81 nm, thus implying the existence of small agglomerates, which could emerge due to the high concentration of MNPs in the buffer solution. The singlet DLS peak is indicative of the high stability of the Fe3O4-PEG3k NP induced by the robust coating formed on the Fe3O4 surface by the PEG3k surface modification [47]. The mean hydrodynamic diameters of EMMSNPs and QCMMSNPs are around 261 nm and 282 nm, respectively, also implying the existence of scattered agglomerates in the buffered solution. The observed difference between the size of EMMSNPs and QCMMSNPs could be attributed to the QC load.

The electrostatic interactions of all types of NPs are directly related to their surface charge, which was analyzed through zeta potential measurements. The PEG3k-surface modification of Fe3O4 NPs resulted in negatively surface-charged Fe3O4-PEG3k NPs (□ 10 ± 1 mV at pH 7.4), implying colloidal stability of the produced PEGylated Fe3O4 NPs in aqueous solution as a result of the electrostatic repulsion between the negatively charged NPs [47,65]. The surface charge of the EMMSNP and QCMMSNP samples, at pH 7.4, was measured to be □ 33 ± 0.67 mV and -40 ± 1.19 mV, respectively. The observed very low zeta-potential values are indicative of enhanced stability and reduced sedimentation and aggregation rates of the corresponding NPs. Furthermore, the extended decrease of zeta-potential compared to that of Fe3O4-PEG3k NPs can be attributed to the large surface charge due to the deprotonation of the Si–OH groups [66,67]. In addition, the observed decrease of zeta-potential of QCMMSNPs compared to that of EMMSNPs can be attributed to the partial deprotonation of QC molecules at the pH of the medium [37,68].

The fact that, in the case of EMMSNPs, the hydrodynamic radius measured by DLS is approximately double the radius measured by TEM, whereas in the case of QCMMSNPs the measured radii with both methods are very close, could be attributed to the increased zeta-potential value of EMMSNPs compared to that of QCMMSNPs. The associated lower electrostatic repulsion between the EMMSNPs may result in greater agglomeration in solution, a fact that could explain the detection by DLS of larger hydrodynamic radii for EMMSNPs.

3.8. BET analysis

N2 sorption measurements were conducted to further determine the pore parameters of EMMSNPs and QCMMSNPs. All physicochemical properties of EMMSNPs and QCMMSNPs are summarized in Table 3, whereas the obtained N2 adsorption–desorption isotherms and pore size distributions are shown in Fig. 8A and B, respectively. Both samples show a typical type IV isotherm with H1 hysteresis loop, indicative of the presence of mesoporosity [69–72]. The observed intense increase in N2 uptake in the relative pressure range between 0.70 and 0.90 for the EMMSNP sample and 0.80–0.95 for the QCMMSNP sample could be attributed to the voids formed between SiO2 NPs [73]. The BJH pore sizes of EMMSNP and QCMMSNP samples were estimated to be 91.50 Å and 168.96 Å, respectively. The BET average pore sizes of EMMSNP and QCMMSNP samples were found to be 150.64 Å and 273.12 Å, respectively. The BET surface areas and pore volumes were estimated to be 169.30 m2•g□ 1 and 0.64 cm3•g□ 1 for the EMMSNP sample, and 108.33 m2•g□ 1 and 0.74 cm3•g□ 1 for the QCMMSNP sample, respectively. It can be concluded that the BET surface area decreases with the encapsulation of QC, whereas the BET average pore size and pore volume increase, thus indicating that the pore size distribution becomes narrow due to the encapsulated QC molecules [74].

Table 3
Summary of physicochemical properties of EMMSNPs and QCMMSNPs.

Sample	Pore size[a] (Å)	Average pore size[b] (Å)	Surface area[c] ($m^2 \bullet g^{-1}$)	Pore volume[d] ($cm^3 \bullet g^{-1}$)
EMMSNPs	91.50	150.64	169.30	0.64
QCMMSNPs	168.96	273.12	108.33	0.74

[a] Calculated from the N_2 BJH adsorption branch.
[b] Calculated from the N_2 BET adsorption branch.
[c] Calculated from the N_2 BET adsorption branch.
[d] Determined from the single point amount adsorbed at $P/P^o = 0.9898$.

3.9. Thermal studies

The thermal decomposition of Fe3O4-PEG3k NPs, EMMSNPs, and QCMMSNPs was studied by TGA under an atmosphere of air (Figs. 9A and B). The Fe3O4-PEG3k NP sample (Fig. 9A) was stable up to 160 ◦C. The observed weight loss of about 10.5%, between 160 ◦C and 322 ◦C could be attributed to the decomposition of the chemisorbed PEG3k molecules. The negligible weight loss of about 0.6% between 322 ◦C and 573 ◦C could be assigned to the Fe3O4-Fe2O3 phase transformation [75]. No further weight loss was observed between 573 ◦C and 800 ◦C. The EMMSNP sample (Fig. 9B) was stable up to 34 ◦C. From that point on, a small weight loss of about 2.3% between 34 ◦C and 147 ◦C was observed, which could be assigned to the loss of the physisorbed water molecules. The observed weight loss of about 13.4% between 147 ◦C and 784 ◦C could be attributed to the decomposition of the chemisorbed PEG3k molecules and the condensation of silanols, which begins at temperatures above 350 ◦C [76]. The QCMMSNP sample (Fig. 9B) was stable up to 17 ◦C. From that point on, a small weight loss of about 3.6% was observed between 17 ◦C and 107 ◦C, which could be assigned to the loss of the physisorbed water molecules. The observed weight loss of about 23.5%, between 107 ◦C and 766 ◦C could be attributed to the decomposition of the chemisorbed PEG3k and encapsulated QC molecules and the condensation of silanols.

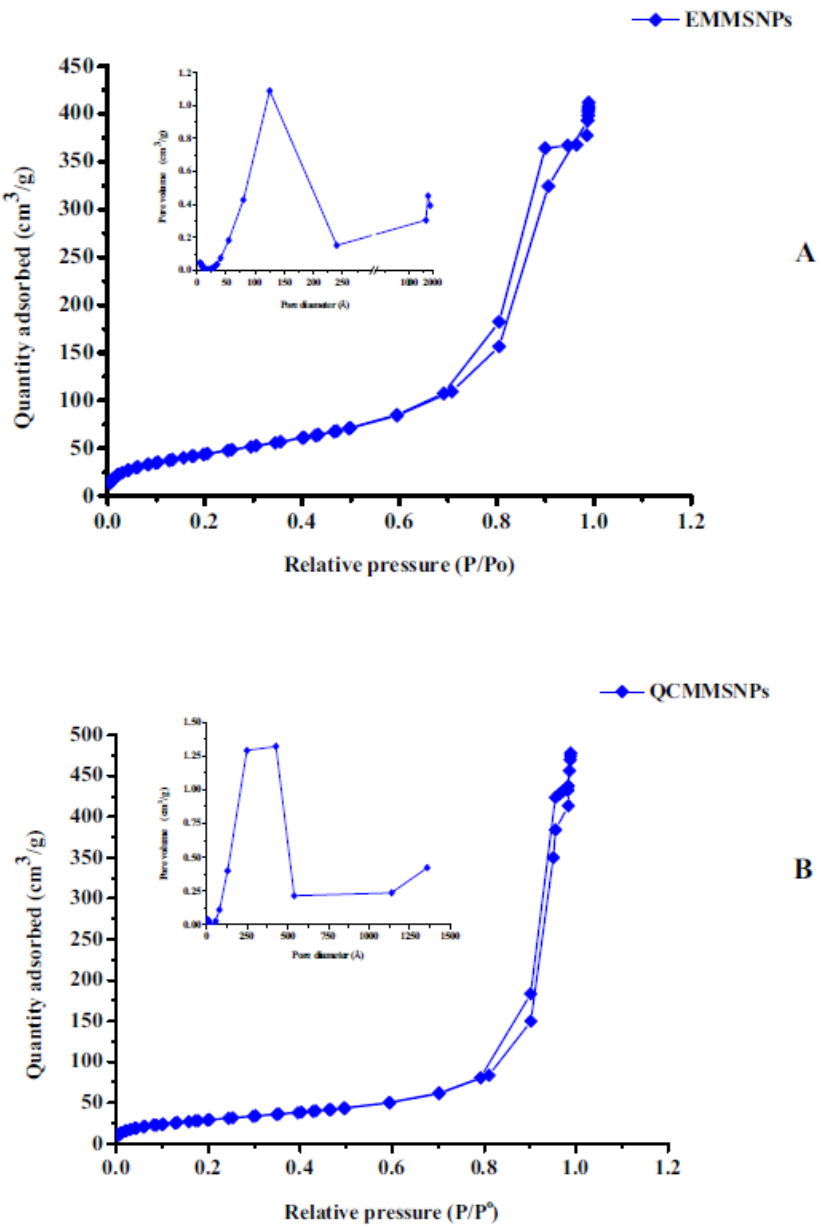

Fig. 8. Nitrogen adsorption-desorption isotherms of **A)** EMMSNPs, and **B)** QCMMSNPs. The inset images show the pore size distribution of each sample.

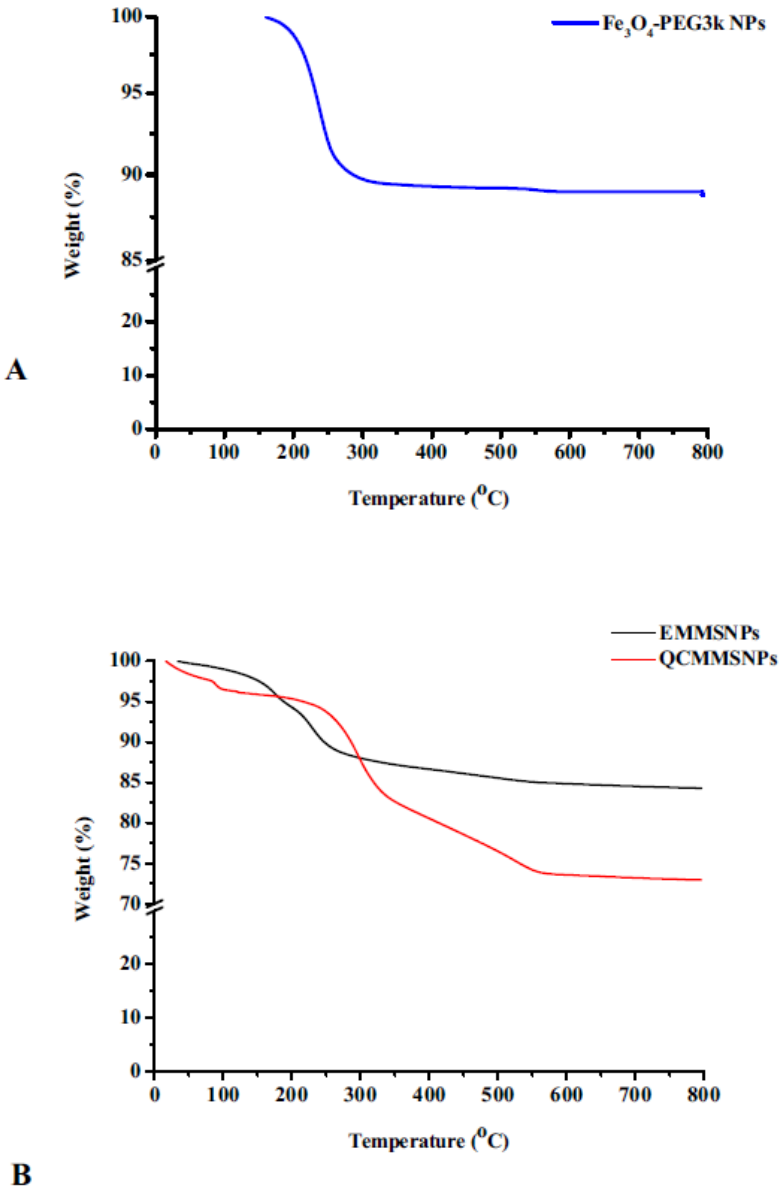

Fig. 9. TGA diagrams of **A)** Fe3O4-PEG3k NPs, and **B)** EMMSNPs (black line), QCMMSNPs (red line).

3.10. Magnetization measurements and determination of Fe3O4 content

Fe3O4-PEG3k NP, EMMSNP and QCMMSNP samples exhibit a strong magnetic response when placed in a magnetic field. At room temperature, magnetization measurements in fields up to 3 T reveal a typical superparamagnetic character (Figs. 10A–C): the magnetic moments within a NP are magnetically coupled and behave as a single super moment. This ensemble aligns easily to any external magnetic field, thus providing high magnetization. In the absence of a magnetic field, the aligned moments of each NP (the “super moment”) fluctuate randomly as a whole due to thermal agitation, since the magnetic anisotropy energy barrier is lower than the thermal energy at room temperature, such that the sample has zero remanence and zero coercivity (inset of Figs. 10A–C). With decreasing temperature, below the superparamagnetic TB, the thermal energy is lower than the energy barrier and the magnetic moments are blocked when the magnetic field is zero or reversed, giving rise to remanence and coercivity. Indeed, coercivity is negligible at room temperature, 3–8 Oe (240–640 $A \cdot m^{-1}$), and the magnetization curve can be fitted to a paramagnetic Langevin function. For the QCMMSNP sample, at 50 K a switching field is required and a hysteresis

loop has been developed (inset of Fig. 10D), with coercivity Hc ~ 120 Oe (9.6 kA·m^{-1}). Superparamagnetic behavior is expected for the given size of the magnetic core, which is lower than the critical size Dsp, for superparamagnetism in iron oxide NPs (Dsp ~ 20–30 nm) [77].

The specific magnetization of the Fe3O4-PEG3k NP sample at the maximum field (3 T) at room temperature is 66.5 emu·g^{-1}. From thermal analysis results (Section 3.9), the estimated content of Fe3O4 in the sample is 89.5%. Since the magnetic moments arise only from Fe3O4, the saturation magnetization of Fe3O4 core NPs is 66.5/89.5% = 74.3 emu·g^{-1}. This value corresponds to 90% of the magnetization of bulk magnetite and the difference, in the case of NPs, is assigned to surface spin disorder that has a stronger influence with diminishing particle size, as previously explained [78]. The EMMSNP sample has a specific saturation magnetization σ = 7.285 emu·g^{-1}. Taking into account the saturation magnetization of Fe3O4 core NPs estimated above (74.3 emu·g^{-1}), Fe3O4 content corresponds to 7.285/74.3 = 9.8% *w*/w of this sample. Accordingly, in the QCMMSNP sample, the Fe3O4 content, estimated from the specific saturation magnetization of the sample, σ = 10.77 emu·g^{-1}, corresponds to 10.77/74.3 = 14.5% w/w of this sample.

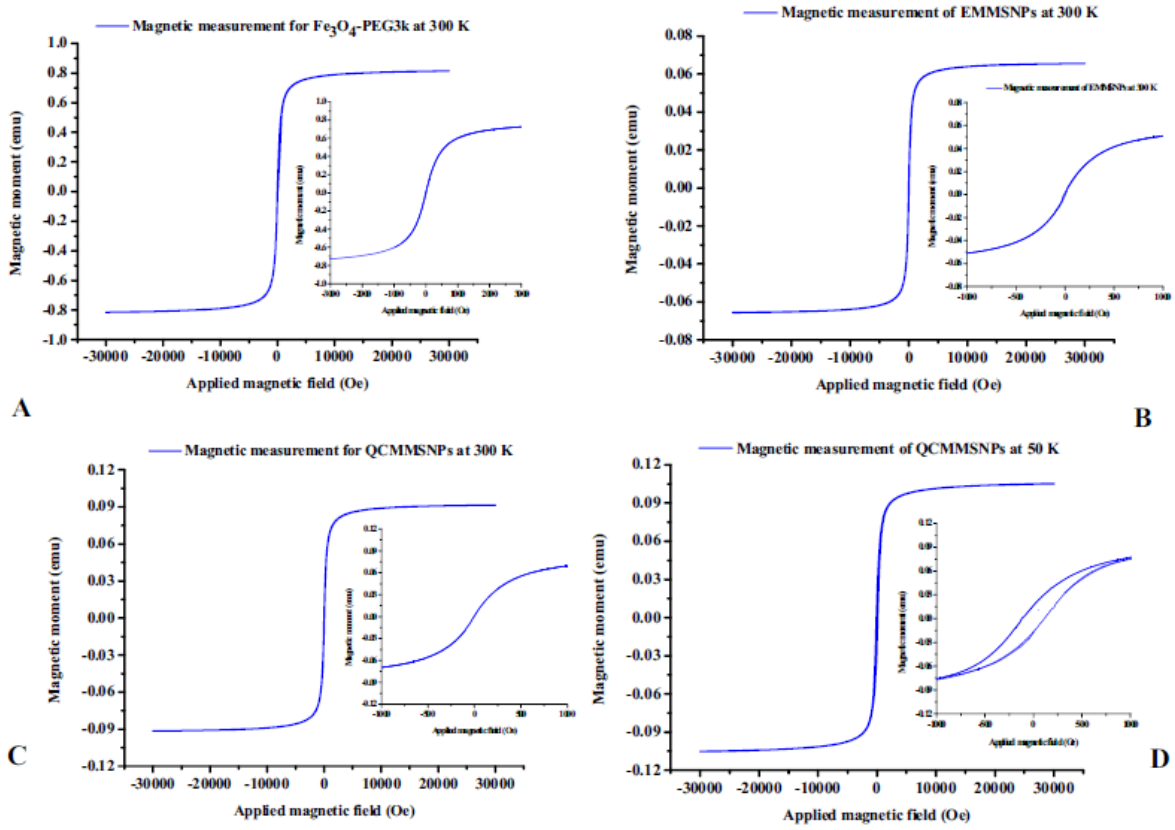

Fig. 10. Magnetization curves of **A)** Fe3O4-PEG3k NPs, **B)** EMMSNPs, **C)** QCMMSNPs at 300 K, and **D)** QCMMSNPs at 50 K. The magnetic field range in the inset graphs is 1000 to +1000 Oe

3.11. QC entrapment efficiency and loading capacity

The in situ entrapment efficiency and loading capacity of QC in QCMMSNPs was estimated to be 70.35% and 14.51%, respectively. The observed relatively high entrapment efficiency and loading capacity, despite the presence of the magnetic core, which occupies considerable volume of the interior of MMSNPs, are probably attributed to the high TEOS-to-QC molar ratio (≈37.9:1) employed in the synthesis of QCMMSNPs and the enhanced host/guest interactions due to intense hydrogen

bond formation between the entrapped flavonoid, the silanol (Si-OH) groups and the PEG3k chains on the surface of the MNPs, thereby promoting a more efficient encapsulation of QC [79–81].

3.12. In vitro QC release study

The release profile of the active encapsulated ingredient (QC), defined by the total amount of QC released and release rate, affects the modulation of the QCMMSNP pharmacokinetic behavior. Fig. 11 shows the percentage of QC released with regard to the total entrapped QC versus time. The equilibrium release percentage of QC from QCMMSNPs, after 48 h of study, was estimated to be around 50.28%. Moreover, the release profile of the encapsulated QC showed that the release rate of the flavonoid was high up to the first 60 min and subsequently decreased significantly, becoming relatively steady after 6 h. This burst of QC release can be attributed to the large surface of the irregularly shaped silica xerogels, the relatively thin outer silica shell compared to the bulky magnetic core, the mesoporous structure of the produced QCMMSNPs, which allows facile penetration of the release medium, as well as the ionization of the silanol groups of the surface and the interior of the pores, which create an ionic environment non-compatible with the hydrophobic nature of QC [37,82].

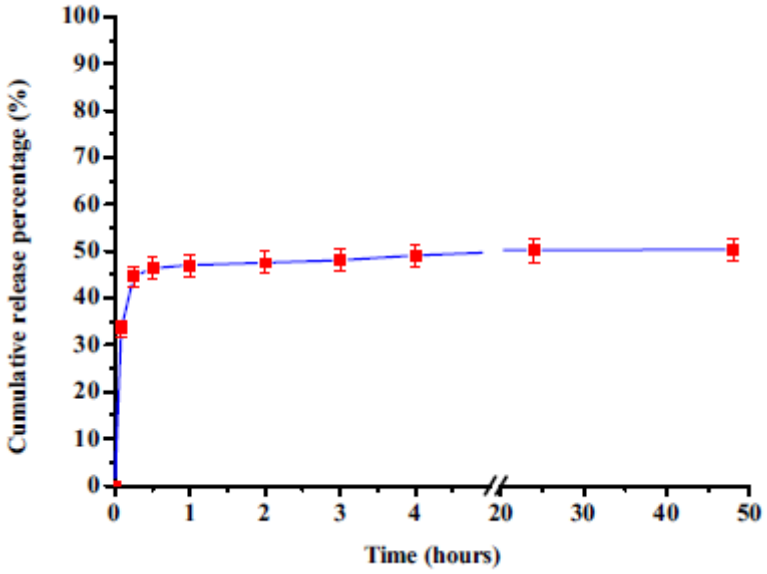

Fig. 11. Cumulative release percentage of QC with regard to the total entrapped QC vs. time.

3.13. Effect of NPs on Aβ aggregation

The potential of the investigated NPs to inhibit aggregation of Aβ40 and formation of amyloid fibrils was studied through circular dichroism spectropolarimetry (CD). The typical aggregation process of Aβ40 produces characteristic CD spectra over time that reflect its transition from random coil (negative maximum at 198 nm) to *β*-sheet (positive maximum at 195 nm and negative maximum at 218 nm) and the gradual formation of larger fibrillar aggregates that precipitate from solution, resulting in loss of the CD signal (Fig. 12A). In the presence of compounds that interact with Aβ and interfere with its aggregation, the typical spectral pattern changes, thereby providing solid experimental evidence for the intervention of the compound in the aggregation process [83].

The effect of plain QC was studied first to serve as reference in the evaluation of the effectiveness of the QC-loaded NPs. In the presence of QC, at ratios of Aβ:QC of 1:0.5 and 1:1, changes are recorded in the aggregation spectra of Aβ (Fig. 12A). At the 1:0.5 ratio, a composite peak gradually develops,

which appears stabilized in solution after day 9 and does not further evolve into insoluble aggregates, typical of solutions of plain Aβ. At the 1:1 ratio, a gradual reduction in the intensity of the initial signal is observed, undergoing no further alterations after day 13. At both Aβ:QC ratios, the thioflavin T (ThT) fluorescence test, that detects mature amyloid fibrils, showed essentially lack of formation of typical fibrils (Fig. 12B). Apparently, the noticeable reduction in the intensity of the CD signal, noted at the 1:1 ratio, is associated with the formation of other types of macromolecular entities that do not behave as typical Aβ fibrils in the ThT test. QC has been shown to inhibit Aβ fibril formation through fluorescence spectroscopic studies and electron microscopy [84,85], however, this is the first time that direct interaction of QC with Aβ and inhibition of fibril formation is demonstrated through CD. Furthermore, the appearance of the CD spectra suggests that, under our conditions, inhibition of fibril formation takes place through interaction of QC with lower-order Aβ species early in the fibrilization process. This finding is in contrast to a literature report, proposing that QC binds to Aβ fibrils at the growing ends [86], in agreement however with the general notion that biophenols interact with Aβ monomers and oligomers of Aβ, blocking its self-assembly into amyloid fibrils [87].

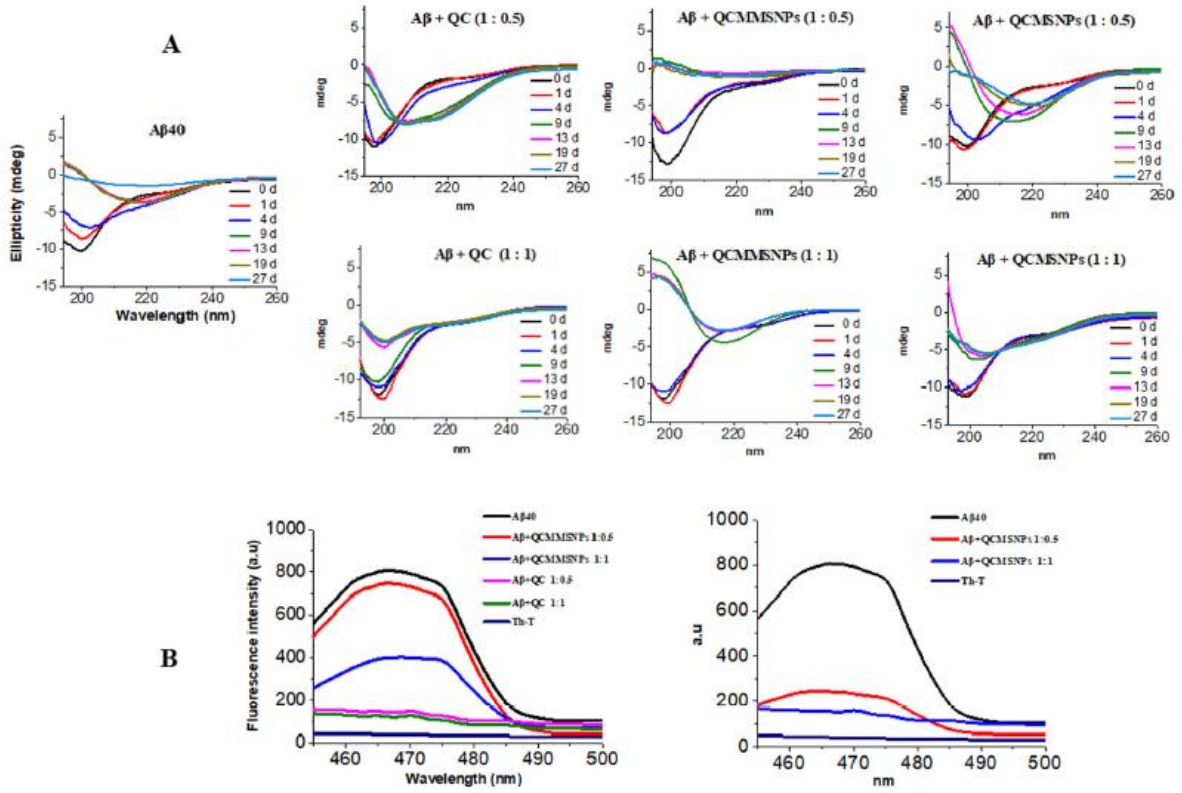

Fig. 12. CD and ThT analysis of the QC-loaded NPs against Aβ aggregation. **A)** CD spectra of 50 μM of Aβ40 in phosphate buffer (PB 10 mM, pH 7.33), in the absence or presence of QCMMSNPs, QCMSNPs, and QC (1:0.5 and 1:1 ratio). Spectra were collected over a period of 27 d at 33 ◦C. Representative spectra from *n* = 3 independent experiments are presented. **B)** Fluorescence spectra of ThT (5 μM in PB 10 mM, pH 7.33) added to Aβ (25 μM) solutions incubated for 27 d, in the absence or presence of QCMMSNPs, QCMSNPs, and QC (1:0.5 and 1:1 ratio). Fluorescence was monitored after excitation at 440 nm. Representative spectra from n = 3 independent experiments are presented.

Next, the action of QCMMSNPs on the aggregation of Aβ was examined, in order to assess their effectiveness as carriers of QC. As the time frame of Aβ aggregation, which proceeds for days under

our conditions, is much larger than the time frame of QC release from QCMMSNPs, which is completed within 1 h under the same conditions (Fig. 11), it is presumed that QC will be available in solution for interaction with Aβ at the early stages of the aggregation process. As can be seen in Fig. 12A, addition of QCMMSNPs at a Aβ:NP ratio of 1:0.5 shows initially a deepening of the negative peak at 198 nm relative to plain Aβ, indicative of interaction. From that point on, it appears that aggregation advances, and at day 9 the CD signal is already reduced to its final value. It appears that at the Aβ:NP 1:0.5 ratio (based on the released QC according to the in vitro release study, vide supra), aggregation of Aβ proceeds faster in the presence of QCMMSNPs and with no visible presence of *β*-sheet formation characterizing the aggregation spectra of Aβ. At the elevated ratio of Aβ:NP 1:1, the *β*-sheet signal is visible at day 9, with a negative maximum at 218 nm, which in the following days appears to be stabilized as no further evolution toward insoluble aggregates takes place apart from a small reduction in its intensity. It should be noted that the CD spectra of QCMMSNPs, in the absence of Aβ, were also obtained over a 27 day period to serve as control and no changes were recorded (Fig. S3, Supplementary Information).

The ThT test (Fig. 12B), which measures the amount of typical amyloid fibrils formed, was subsequently performed on all CD samples [44]. As can be seen, it shows noticeable reduction in the amount of fibrils formed in the case of the Aβ:NP ratio of 1:0.5, which becomes even more significant at the Aβ:NP 1:1 ratio, in agreement with the CD data. It is evident from the data that QCMMSNPs are active against Aβ aggregation. However, before reaching a well-defined conclusion on the contribution of released QC, it was necessary to evaluate the effect of EMMSNPs on Aβ aggregation. Interestingly enough, EMMSNPs have an effect on the aggregation course of Aβ, even in the absence of QC (Fig. S4, Supplementary Information). Their presence results in changes of the typical appearance of the Aβ aggregation profile, denoting interaction. As can be seen (Fig. S4, Supplementary Information), the end result is loss of signal, indicating aggregate formation, a fact that was also confirmed through the ThT test, which showed formation of typical amyloid fibrils (Fig. S5, Supplementary Information). Therefore, in the presence of QCMMSNPs, interaction takes place with both the MNPs and the released QC, however, the reduction in fibril formation can only be ascribed to QC, based on solid evidence from CD and ThT data.

For comparative purposes, the interaction of non-magnetized QCMSNPs synthesized and evaluated against oxidative stress in neurodegeneration [37] was also studied through CD. As observed in the case of the MNPs, QCMSNPs are definitely active against Aβ aggregation (Fig. 12A). At the lower Aβ:NP ratio of 1:0.5 [37], QCMSNPs stabilize *β*-sheet-like formation that does not proceed any further, whereas at the higher ratio of 1:1, composite peaks between random coil and *β*-sheet remain in solution with no further advancement. The ThT test showed great reduction in fibril formation at the 1:0.5 ratio and complete inhibition at the 1:1 ratio (Fig. 12B). The effect of EMSNPs was also evaluated and, as in the case of MNPs, it appears that there is interaction with Aβ (Figs. S4 and S5, Supplementary Information), which however does not inhibit fibril formation.

Comparison of our data on QCMMSNPs and QCMSNPs, clearly shows that the amount of QC present in solution plays a role, since in all cases, inhibition of aggregation is greater at the 1:1 ratio, where more QC is present. Increasing the relative concentration of QCMMSNPs relative to the Aβ (based on the released QC according to the in vitro release study, vide supra) in order to increase the amount of available QC, was not successful, as the aggregating effect of QCMMSNPs overwhelms the inhibitory effect of QC and rapid aggregation and fibril formation is observed, as demonstrated with ThT and CD studies at the Aβ:NP ratios of 1:2 and 1:3 (Figs. S5 and S6, Supplementary Information).

Furthermore, it is clear from the data that the availability of QC in the beginning of the aggregation process, results in a more effective inhibition of fibril formation. At the 50 μM concentration,

employed for the 1:1 ratio studies, plain QC results in complete inhibition of fibril formation, QCMSNPs (release study) [37] exhibit again complete inhibition of fibril formation, whereas QCMMSNPs (Section 3.12) inhibit fibril formation to a lesser extent (Fig. 12B). The fact that early presence of QC totally prevents fibril formation further supports our contention that interaction of QC takes place with lower order aggregates of Aβ.

3.14. Rescue of primary neuronal cells from Aβ toxicity

The capacity of the NPs, under investigation, to rescue cells from Aβ toxicity was measured through the MTT assay, which is widely used in neurotoxicity studies of aggregating peptides [88]. As shown in Fig. 13A, exposure of primary hippocampal neurons to Aβ40 (1 μM) reduces cell viability to 67% of untreated cells. This reduction is in accordance with values reported in the literature for Aβ40 toxicity in primary neurons [89]. The presence of QCMMSNPs in the Aβ solution rescues cells from Aβ toxicity and raises viability to 70.3% for the Aβ:NP 1:0.5 ratio and 85.2% for the Aβ:NP 1:1 ratio (Fig. 13A), resulting in rescue effects of 4.5% and 26.9%, respectively. The rise in viability is much more intense in the presence of QCMSNPs, with rescue effects reaching 26.9% for the Aβ:NP 1:0.5 ratio and 34.3% for the 1:1 ratio [37]. As expected from its known anti-aggregation properties [62,90], which were confirmed through CD spectroscopy, plain QC raised the viability of primary hippocampal neurons, resulting in rescue effects of 37.3% and 43.3% for the Aβ:QC 1:0.5 and 1:1, respectively. It is clear from the above data that the exerted rescue effect depends on the amount of QC present in solution, however, further increase in the relative amount of NPs compared to Aβ was not attempted, as 1 μM of QCMSNPs and EMSNPs [37] exhibit moderate cytotoxicity even in the absence of Aβ (Fig. 13A). Even though direct comparisons cannot be made, this cytotoxicity is within the range of the cytotoxicity values reported for NPs of various compositions in primary cells [91].

3.15. Intracellular ROS measurements

The effect of NPs, under evaluation, on ROS generation induced by Aβ40 in primary hippocampal neurons was examined and the results are summarized in Fig. 13B. Exposure of the cells to 1 μM Aβ40 for 24 h resulted in a burst of ROS production as evidenced by the 10-fold increase in the fluorescence of the DCF dye generated from the reaction of its non-fluorescent precursor with peroxo radicals [92]. This increase is in accordance with literature data [93]. Co-incubation with QCMMSNPs at Aβ40:NP ratios of 1:0.5 and 1:1 (based on the released QC according to the in vitro release study, vide supra) decreases the generated DCF fluorescence by 17.1% and 28.8%, respectively, the reduction being even more noticeable in the case of QCMSNPs with values of 36.9% and 41.4% for the same ratios. Under our conditions, the presence of plain QC resulted in reduction of fluorescence by 45.4% for the Aβ:QC 1:0.5 ratio and 53.2% for the Aβ:QC 1:1 ratio, in agreement with literature data [94]. It is obvious from the data that both types of QC-loaded NPs have a great impact on ROS formation with the Aβ40:NP 1:1 ratio, which is associated with a higher amount of QC in solution, being the one most effective. Our control experiments with all nanoparticles employed in the study (QCMSNPs, QCMMSNPs, Fig. 13B, and the Fe3O4-PEG3k NPs, Fig. S7, Supplementary Information) indicate that all antioxidant action recorded in the presence of Aβ is associated with released QC and not the nanocarrier itself. As in the cytotoxicity studies, a higher proportion of NPs compared to Aβ was not attempted, as the NPs themselves induce generation of ROS to a limited extent (Fig. 13B).

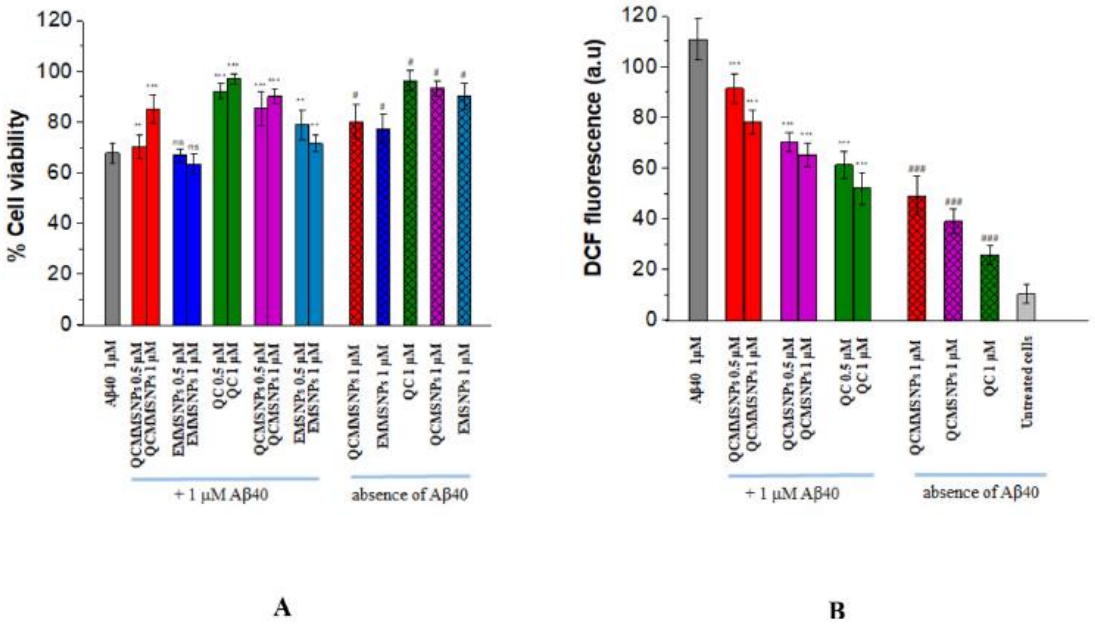

A B

Fig. 13. Aβ-induced cell toxicity and oxidative stress studies. **A)** Effects of 0.5 and 1 μM of QCMMSNPs, QCMSNPs, and QC on the cytotoxicity of 1 μM Aβ40, in primary mouse hippocampal neurons, after 24 h of incubation at 37 ◦C. Cell viability was assessed using the MTT assay (n = 3 independent experiments, each one performed in six replicates). **B)** Effect of 1 μM of QCMMSNPs, QCMSNPs, and QC on Aβ40 (1 μM) induced ROS generation in primary mouse hippocampal neurons, after 24 h of incubation at 37 ◦C. ROS levels were measured by DCF fluorescence assay (n = 3 independent experiments, each one performed in six replicates). The data are presented as mean ± SEM, $*p \leq 0.05$, $**p \leq 0.01$, $***p \leq 0.001$, ns (not significant) > 0.05 compared to Aβ40 (1 μM) treatment and $\#p < 0.01$ and $\#\#p < 0.01$, $\#\#\#p < 0.001$ compared to control (untreated cells).

4. Conclusions

In pursuit of development of advanced NP-based drug formulations as stable, long-life and bioavailable nanocarriers of natural flavonoids, novel QC-loaded modified magnetic core-shell mesoporous silica nano-formulations were synthesized, physicochemically characterized and biologically evaluated in anti-amyloid and antioxidant assays. The hybrid nanocarriers showed exceptional stability in physiological media and exhibited enhanced solubility of the encapsulated QC compared to the free flavonoid, as evidenced through entrapment efficiency and loading capacity results, and in vitro release studies, data that imply increased bioavailability of the QC load. Furthermore, the generated MMSNPs preserved the superparamagnetic behavior of the employed surface-modified MNP core, an advantageous feature for magnetic targeting applications. Examination of their biological properties revealed that released QC retains its antioxidant and anti-amyloid properties, showing that nano-encapsulation does not affect the multifaceted bioactivity of QC. The biological evaluation studies, based on two important properties of QC, serve as proof of concept on the feasibility of magnetically directed on-site release of active QC to exert its multitude of pharmacological activities. Collectively, the present work projects the ability of MMSNPs to function as efficient nanocarriers of bioactive flavonoids and sets the stage for further development of advanced magnetic nano-platforms for targeted therapeutic applications.

References

[1] K. Chatterjee, S. Sarkar, K.J. Rao, S. Paria, Core/shell nanoparticles in biomedical applications, Adv. Colloid Interf. Sci. 209 (2014) 8–39, https://doi.org/10.1016/j. cis.2013.12.008.

[2] M.A. Busquets, R. Sabat´e, J. Estelrich, Potential applications of magnetic particles to detect and treat Alzheimer's disease, Nanoscale Res. Lett. 9 (2014) 538, https:// doi.org/10.1186/1556-276X-9-538.

[3] S. Parveen, S.K. Sahoo, Nanomedicine: clinical applications of polyethylene glycol conjugated proteins and drugs, Clin. Pharmacokinet. 45 (2006) 965–988, https:// doi.org/10.2165/00003088-200645100-00002.

[4] C. Roney, P. Kulkarni, V. Arora, P. Antich, F. Bonte, A. Wu, N.N. Mallikarjuana, S. Manohar, H.F. Liang, A.R. Kulkarni, H.W. Sung, M. Sairam, T.M. Aminabhavi, Targeted nanoparticles for drug delivery through the blood-brain barrier for Alzheimer's diseases, J. Control. Release 108 (2005) 193–214, https://doi.org/ 10.1016/j.jconrel.2005.07.024.

[5] P. Blasi, S. Giovagnoli, A. Schoubben, M. Ricci, C. Rossi, Solid lipid nanoparticles for targeted brain drug delivery, Adv. Drug Deliv. Rev. 59 (2007) 454–477, https:// doi.org/10.1016/j.addr.2007.04.011.

[6] A. Kumari, S.K. Yadav, S.C. Yadav, Biodegradable polymeric nanoparticles based drug delivery systems, Colloids Surf. B: Biointerfaces 75 (2010) 1–18, https://doi. org/10.1016/j.colsurfb.2009.09.001.

[7] I. Zhang, F.X. Gu, J.M. Chan, A.Z. Wang, R.S. Langer, O.C. Farokhzad, Nanoparticles in medicine: therapeutic applications and developments, Clin. Pharmacol. Ther. 83 (2008) 761–769, https://doi.org/10.1038/sj.clpt.6100400.

[8] N. Sounderya, Y. Zhang, Use of core/shell structured nanoparticles for biomedical applications, Recent Pat. Biomed. Eng. 1 (2008) 34–42, https://doi.org/10.2174/ 1874764710801010034.

[9] J.M. Rosenholm, C. Sahlgren, M. Linden, Multifunctional mesoporous silica nanoparticles for combined therapeutic, diagnostic and targeted action in cancer treatment, Curr. Drug Targets 12 (2011) 1166–1186, https://doi.org/10.2174/ 138945011795906624.

[10] Y. Wang, Q. Zhao, N. Han, L. Bai, J. Li, J. Liu, E. Che, L. Hu, Q. Zhang, T. Jiang, S. Wang, Mesoporous silica nanoparticles in drug delivery and biomedical applications, Nanomedicine: NBM 11 (2015) 313–327, https://doi.org/10.1016/j. nano.2014.09.014.

[11] Y. Chen, H. Chen, J. Shi, Drug delivery/imaging multifunctionality of mesoporous silica-based composite nanostructures, Expert Opin. Drug Deliv. 11 (2014) 917–930, https://doi.org/10.1517/17425247.2014.908181.

[12] H. Baghirov, D. Karaman, T. Viitala, A. Duchanoy, Y.R. Lou, V. Mamaeva, E. Pryazhnikov, L. Khiroug, C. de Lange Davies, C. Sahlgren, J.M. Rosenholm, Feasibility study of the permeability and uptake of mesoporous silica nanoparticles across the blood-brain barrier, PLoS One 11 (2016) e0160705, https://doi.org/ 10.1371/journal.pone.0160705.

[13] Q. He, Z. Zhang, Y. Gao, J. Shi, Y. Li, Intracellular localization and cytotoxicity of spherical mesoporous silica nano- and microparticles, Small 5 (2009) 2722–2729, https://doi.org/10.1002/smll.200900923.

[14] A.S. Lübbe, C. Alexiou, C. Bergemann, Clinical applications of magnetic drug targeting, J. Surg. Res. 95 (2001) 200–206, https://doi.org/10.1006/ jsre.2000.6030.

[15] Y.W. Jun, J.H. Lee, J. Cheon, Chemical design of nanoparticle probes for high-performance magnetic resonance imaging, Angew. Chem. Int. Ed. 47 (2008) 5122–5135, https://doi.org/10.1002/anie.200701674.

[16] H.B. Na, I.C. Song, T. Hyeon, Inorganic nanoparticles for MRI contrast agents, Adv. Mater. 21 (2009) 2133–2148, https://doi.org/10.1002/adma.200802366.

[17] C. Corot, P. Robert, J.M. Idee, M. Port, Recent advances in iron oxide nanocrystal technology for medical imaging, Adv. Drug Deliv. Rev. 58 (2006) 1471–1504, https://doi.org/10.1016/j.addr.2006.09.013.

[18] O. Veiseh, J.W. Gunn, M.Q. Zhang, Design and fabrication of magnetic nanoparticles for targeted drug delivery and imaging, Adv. Drug Deliv. Rev. 62 (2010) 284–304, https://doi.org/10.1016/j.addr.2009.11.002.

[19] J. Chomoucka, J. Drbohlavova, D. Huska, V. Adam, R. Kizek, J. Hubalek, Magnetic nanoparticles and targeted drug delivering, Pharmacol. Res. 62 (2010) 144–149, https://doi.org/10.1016/j.phrs.2010.01.014.

[20] A.K. Gupta, M. Gupta, Synthesis and surface engineering of iron oxide nanoparticles for biomedical applications, Biomaterials 26 (2005) 3995–4021, https://doi.org/10.1016/j.biomaterials.2004.10.012.

[21] M. Mahmoudi, S. Sant, B. Wang, S. Laurent, T. Sen, Superparamagnetic iron oxide nanoparticles (SPIONs): development, surface modification and applications in chemotherapy, Adv. Drug Deliv. Rev. 63 (2011) 24–46, https://doi.org/10.1016/j. addr.2010.05.006.

[22] D.L. Thorek, A.K. Chen, J. Czupryna, A. Tsourkas, Superparamagnetic iron oxide nanoparticle probes for molecular imaging, Ann. Biomed. Eng. 34 (2006) 23–38, https://doi.org/10.1007/s10439-005-9002-7.

[23] L. Tang, J. Cheng, Nonporous silica nanoparticles for nanomedicine application, Nano Today 8 (2013) 290–312, https://doi.org/10.1016/j.nantod.2013.04.007.

[24] M. Fiorani, A. Guidarelli, M. Blasa, C. Azzolini, M. Candiracci, E. Piatti, O. Cantoni, Mitochondria accumulate large amounts of quercetin: prevention of mitochondrial damage and release upon oxidation of the extramitochondrial fraction of the flavonoid, J. Nutr. Biochem. 21 (2010) 397–404, https://doi.org/10.1016/j. jnutbio.2009.01.014.

[25] V. Cody, Iodothyronine deiodinase is inhibited by plant flavonoids, Prog. Clin. Biol. Res. 213 (1986) 359–371.

[26] V. Cody, Plant flavonoids in biology and medicine II: biochemical, cellular, and medicinal properties, Prog. Clin. Biol. Res. 280 (1988) 341–344.

[27] A. Priprem, J. Watanatorn, S. Sutthiparinyanont, W. Phachonpai, S. Muchimapura, Anxiety and cognitive effects of quercetin liposomes in rats, Nanomedicine 4 (2008) 70–78, https://doi.org/10.1016/j.nano.2007.12.001.

[28] M. Kanter, C. Unsal, C. Aktas, M. Erboga, Neuroprotective effect of quercetin against oxidative damage and neuronal apoptosis caused by cdmium in hippocampus, Toxicol. Ind. Health 32 (2016) 541–550, https://doi.org/10.1177/ 0748233713504810.

29] S.M. Choi, B.C. Kim, Y.H. Cho, K.H. Choi, J. Chang, M.S. Park, M.K. Kim, K.H. Cho, J.K. Kim, Effects of flavonoid compounds on β-amyloid-peptide-induced neuronal death in cultured mouse cortical neurons, Chonnam. Med. J. 50 (2014) 45–51, https://doi.org/10.4068/cmj.2014.50.2.45.

[30] C.M. Liu, G.H. Zheng, C. Cheng, J.M. Sun, Quercetin protects mouse brain against lead-induced neurotoxicity, J. Agric. Food Chem. 61 (2013) 7630–7635, https:// doi.org/10.1021/jf303387d.

[31] M.A. Ansari, H.M. Abdul, G. Joshi, W.O. Opii, D.A. Butterfield, Protective effect of quercetin in primary neurons against Abeta(1-42): relevance to Alzheimer's disease, J. Nutr. Biochem. 20 (2009) 269–275, https://doi.org/10.1016/j. jnutbio.2008.03.002.

[32] M. Stefani, S. Rigacci, Protein folding and aggregation into amyloid: the interference by natural phenolic compounds, Int. J. Mol. Sci. 14 (2013) 12411–12457, https://doi.org/10.3390/ijms140612411.

[33] J. Hao, B. Guo, S. Yu, W. Zhang, D. Zhang, J. Wang, Y. Wang, Encapsulation of the flavonoid quercetin with chitosan-coated nano-liposomes, LWT-Food Sci. Technol. 85 (2017) 37–44, https://doi.org/10.1016/j.lwt.2017.06.048.

[34] T. Toniazzo, M.S. Peres, A.P. Ramos, S.C. Pinho, Encapsulation of quercetin in liposomes by ethanol injection and physicochemical characterization of dispersions and lyophilized vesicles, Food Biosci. 19 (2017) 17–25, https://doi.org/10.1016/j. fbio.2017.05.003.

[35] O. Lozano, A. L´azaro-Alfaro, C. Silva-Platas, Y. Oropeza-Almaz´an, A. Torres- Quintanilla, J. Bernal-Ramírez, H. Alves-Figueiredo, G. García-Rivas, Nanoencapsulated quercetin improves cardioprotection during hypoxia-reoxygenation injury through preservation of mitochondrial function, Oxidative Med. Cell. Longev. 2019 (2019), 7683051, https://doi.org/10.1155/2019/ 7683051.

[36] A. Praveena, S. Prabu, R. Rajamohan, Encapsulation of quercetin in β-cyclodextrin and (2-hydroxypropyl)-β-cyclodextrin cavity: in-vitro cytotoxic evaluation, J. Macromol. Sci. A 54 (2017) 894–901, https://doi.org/10.1080/ 10601325.2017.1381851.

[37] C.M. Nday, E. Halevas, G.E. Jackson, A. Salifoglou, Quercetin encapsulation in modified silica nanoparticles: potential use against Cu(II)-induced oxidative stress in neurodegeneration, J. Inorg. Biochem. 145 (2015) 51–64, https://doi.org/ 10.1016/j.jinorgbio.2015.01.001.

[38] S.L. Vidal, C. Rojas, R.B. Padín, M.P. Rivera, A. Haensgen, M. Gonz´alez, S. Rodríguez-Llamazares, Synthesis and characterization of polyhydroxybutyrate-*co*-hydroxyvalerate nanoparticles for encapsulation of quercetin, J. Bioact. Compat. Polym. 31 (2016) 439–452, https://doi.org/10.1177/ 0883911516635839.

[39] X. Gao, B. Wang, X. Wei, K. Men, F. Zheng, Y. Zhou, Y. Zheng, M. Gou, M. Huang, G. Guo, N. Huang, Z. Qian, Y. Wei, Anticancer effect and mechanism of polymer micelle-encapsulated quercetin on ovarian cancer, Nanoscale 4 (2012) 7021–7030, https://doi.org/10.1039/C2NR32181E.

[40] P. Vashisth, K. Nikhil, S.C. Pemmaraju, P.A. Pruthi, V. Mallick, H. Singh, A. Patel, N.C. Mishra, R.P. Singh, V. Pruthi, Antibiofilm activity of quercetin-encapsulated cytocompatible nanofibers against

Candida albicans, J. Bioact. Compat. Polym. 28 (2013) 652–665, https://doi.org/10.1177/0883911513502279.

[41] H. Pool, S. Mendoza, H. Xiao, D.J. McClements, Encapsulation and release of hydrophobic bioactive components in nanoemulsion-based delivery systems: impact of physical form on quercetin bioaccessibility, Food Funct. 4 (2013) 162–174, https://doi.org/10.1039/C2FO30042G.

[42] J.C. Colas, W. Shi, V.S.N. Malleswara Rao, A. Omri, M. Reza Mozafari, H. Singh, Microscopical investigations of nisin-loaded nanoliposomes prepared by Mozafari method and their bacterial targeting, Micron 38 (2007) 841–847, https://doi.org/ 10.1016/j.micron.2007.06.013.

[43] T. Andrade-Filho, T.C.S. Ribeiro, J. Del Nero, The UV-vis absorption spectrum of the flavonol quercetin in methanolic solution: a theoretical investigation, Eur. Phys. J. E29 (2009) 253–259, https://doi.org/10.1140/epje/i2009-10485-7.

[44] I. Matis, D.C. Delivoria, B. Mavroidi, N. Papaevgeniou, S. Panoutsou, S. Bellou, K. D. Papavasileiou, Z.I. Linardaki, A.V. Stavropoulou, K. Vekrellis, N. Boukos, F. N. Kolisis, E.S. Gonos, M. Margarity, M.G. Papadopoulos, S. Efthimiopoulos, M. Pelecanou, N. Chondrogianni, G. Skretas, An integrated bacterial system for the discovery of chemical rescuers of disease-associated protein misfolding, Nat. Biomed. Eng. 1 (2017) 838–852, https://doi.org/10.1038/s41551-017-0144-3.

[45] R. Massart, Preparation of aqueous magnetic liquids in alkaline and acidic media, IEEE Trans. Magn. 17 (1981) 1247–1248, https://doi.org/10.1109/ TMAG.1981.1061188.

[46] S. Lefebure, E. Dubois, V. Cabuil, S. Neveu, R. Massart, Monodisperse magnetic nanoparticles: preparation and dispersion in water and oils, J. Mater. Res. 13 (1998) 2975–2981, https://doi.org/10.1557/JMR.1998.0407.

[47] A. Mukhopadhyay, N. Joshi, K. Chattopadhyay, G. De, A facile synthesis of PEG-coated magnetite (Fe3O4) nanoparticles and their prevention of the reduction of cytochrome c, ACS Appl. Mater. Interfaces 4 (2012) 142–149, https://doi.org/ 10.1021/am201166m.

[48] S.K. Milonji´c, M.M. Kopeˇcni, Z.E. Ili´c, The point of zero charge and adsorption properties of natural magnetite, J. Radioanal. Chem. 78 (1983) 15–24, https://doi. org/10.1007/BF02519745.

[49] D.J. Wesolowski, M.L. Machesky, D.A. Palmer, L.M. Anovitz, Magnetite surface charge studies to 290◦C from *in situ* pH titrations, Chem. Geol. 167 (2000) 193–229, https://doi.org/10.1016/S0009-2541(99)00209-0.

[50] G.A. Parks, The isoelectric points of solid oxides, solid hydroxides, and aqueous hydroxo complex systems, Chem. Rev. 65 (1965) 177–198, https://doi.org/ 10.1021/cr60234a002.

[51] H. Tamura, N. Katayama, R. Furuichi, Modeling of ion-exchange reactions on metal oxides with the Frumkin isotherm. 1. Acid base and charge characteristics of MnO2, TiO2, Fe3O4, and Al2O3 surfaces and adsorption affinity of alkali metal ions,

[52] Z. Sun, F. Su, W. Forsling, P. Samskog, Surface characteristics of magnetite in aqueous suspension, J. Colloid Interface Sci. 197 (1998) 151–159, https://doi.org/ 10.1006/jcis.1997.5239.

[53] M. Elisa de Sousa, M.B. Fern´andez van Raap, P.C. Rivas, P. Mendoza Z´elis, P. Girardin, G.A. Pasquevich, J.L. Alessandrini, D. Muraca, F.H. S´anchez, Stability and relaxation mechanisms of citric acid coated magnetite nanoparticles for magnetic hyperthermia, J. Phys. Chem. C 117 (2013) 5436–5445, https://doi.org/ 10.1021/jp311556b.

[54] C. Barrera, A. Herrera, Y. Zayas, C. Rinaldi, Surface modification of magnetite nanoparticles for biomedical applications, J. Magn. Magn. Mater. 321 (2009) 1397–1399, https://doi.org/10.1016/j.jmmm.2009.02.046.

[55] L. Guerrini, R.A. Alvarez-Puebla, N. Pazos-Perez, Surface modifications of nanoparticles for stability in biological fluids, Mater. (Basel) 11 (2018) E1154, https://doi.org/10.3390/ma11071154.

[56] S. Gil, E. Castro, J.F. Mano, Synthesis and characterization of stable dicarboxylic pegylated magnetite nanoparticles, Mater. Lett. 100 (2013) 266–270, https://doi. org/10.1016/j.matlet.2013.03.058.

[57] L.L. Hench, J.K. West, The sol-gel process, Chem. Rev. 90 (1990) 33–72, https:// doi.org/10.1021/cr00099a003.

[58] V.B. Kandimalla, V.S. Tripathi, H. Ju, Immobilization of biomolecules in sol–gels: biological and analytical applications, Crit. Rev. Anal. Chem. 36 (2006) 73–106, https://doi.org/10.1080/10408340600713652.

[59] A.K. Gupta, S. Wells, Surface-modified superparamagnetic nanoparticles for drug delivery: preparation, characterization, and cytotoxicity studies, IEEE Trans. Nanosci. 3 (2004) 66–73, https://doi.org/10.1109/TNB.2003.820277.

[60] J.Y. Park, D. Patel, G.H. Lee, S. Woo, Y. Chang, Highly water-dispersible PEG surface modified ultra small superparamagnetic iron oxide nanoparticles useful for target-specific biomedical applications, Nanotechnology 19 (2008) 365603, https://doi.org/10.1088/0957-4484/19/36/365603.

[61] H. Elimelech, D. Avnir, Sodium-silicate route to submicrometer hybrid PEG@silica particles, Chem. Mater. 20 (2008) 2224–2227, https://doi.org/10.1021/ cm703215r.

[62] A.R. Kiasat, S. Nazari, J. Davarpanah, Facile synthesis of an organic–inorganic nanocomposite, PEG–silica, by sol–gel method; its characterization and application as an efficient catalyst in regioselective nucleophilic ring opening of epoxides: preparation of β-azido alcohols and β-cyanohydrins, C. R. Chimie 17 (2014) 124–130, https://doi.org/10.1016/j.crci.2013.07.008.

[63] T. Pralhad, K. Rajendrakumar, Study of freeze-dried quercetin–cyclodextrin binary systems by DSC, FT-IR, X-ray diffraction and SEM analysis, J. Pharm. Biomed. Anal. 34 (2004) 333–339, https://doi.org/10.1016/S0731-7085(03)00529-6.

[64] V. Natarajan, N. Krithica, B. Madhan, P.K. Sehgal, Formulation and evaluation of quercetin polycaprolactone microspheres for the treatment of rheumatoid arthritis, J. Pharm. Sci. 100 (2011) 195–205, https://doi.org/10.1002/jps.22266.

[65] C. Nazli, T.I. Ergenc, Y. Yar, H.Y. Acar, S. Kizilel, RGDS-functionalized polyethylene glycol hydrogel-coated magnetic iron oxide nanoparticles enhance specific intracellular uptake by HeLa cells, Int. J. Nanomedicine 7 (2012) 1903–1920, https://doi.org/10.2147/IJN.S29442.

[66] K. Gdula, A. Dąbrowski, E. Skwarek, Synthesis, surface characterization and electrokinetic properties of colloidal silica nanoparticles with magnetic core, Adsorption 22 (2016) 681–688, https://doi.org/10.1007/s10450-015-9755-8.

[67] L. Mandi´c, A. Sadˇzak, V. Strasser, G. Baranovi´c, D.D. Juraˇsin, M.D. Sikiri´c, S. ˇSegota, Enhanced protection of biological membranes during lipid peroxidation: study of the interactions between flavonoid loaded mesoporous silica nanoparticles and model cell membranes, Int. J. Mol. Sci. 20 (2019) 2709–2731, https://doi.org/ 10.3390/ijms20112709.

[68] R. Amorati, A. Baschieri, A. Cowden, L. Valgimigli, The antioxidant activity of quercetin in water solution, Biomimetics 2 (2017) 9, https://doi.org/10.3390/ biomimetics2030009.

[69] E. Gianotti, C.A. Bertolino, C. Benzi, G. Nicotra, G. Caputo, R. Castino, C. Isidoro, S. Coluccia, Photoactive hybrid nanomaterials: indocyanine immobilized in mesoporous MCM-41 for "in-cell" bioimaging, ACS Appl. Mater. Interfaces 1 (2009) 678–687, https://doi.org/10.1021/am800196r.

[70] A. Molinari, A. Maldotti, A. Bratovcic, G. Magnacca, Fe(III)-porphyrin heterogenized on MCM-41: matrix effects on the oxidation of 1,4-pentanediol, Catal. Today 161 (2011) 64–69, https://doi.org/10.1016/j.cattod.2010.09.004.

[71] K.S.W. Sing, D.H. Everett, R.A.W. Haul, L. Moscou, R.A. Piertti, J. Rouqu`erol, T. Siemieniewska, Reporting physisorption data for gas/solid systems with special reference to the determination of surface area and porosity (Recommendations 1984), Pure Appl. Chem. 57 (1985) 603–619, https://doi.org/10.1351/ pac198557040603.

[72] Z.A. Alothman, A review: fundamental aspects of silicate mesoporous materials, Mater. (Basel) 5 (2012) 2874–2902, https://doi.org/10.3390/ma5122874.

[73] Y. Han, J.Y. Ying, Generalized fluorocarbon-surfactant-mediated synthesis of nanoparticles with various mesoporous structures, Angew. Chem.

[74] X. Du, J. He, Regulation role of ibuprofen toward the morphology of porous silica nanospheres during its in situ encapsulation, J. Colloid Interface Sci. 345 (2010) 269–277, https://doi.org/10.1016/j.jcis.2010.02.012.

[75] S. Nigam, K.C. Barick, D. Bahadur, Development of citrate-stabilized Fe3O4 nanoparticles: conjugation and release of doxorubicin for therapeutic applications, J. Magn. Magn. Mater. 323 (2011) 237–243, https://doi.org/10.1016/j. jmmm.2010.09.009.

[76] R.F. de Farias, C. Airoldi, Effect of addition of divalent transition metal chlorides on the structure and thermal stability of lamellar silica synthesized by the neutral amine route, J. Therm. Anal. 53 (1998) 751, https://doi.org/10.1006/ jssc.1999.8504.

[77] K.M. Krishnan, Biomedical nanomagnetics: a *spin* through possibilities in imaging, diagnostics, and therapy, IEEE Trans. Magn. 7 (2010) 2523–2558, https://doi.org/ 10.1109/TMAG.2010.2046907.

[78] E. Halevas, B. Mavroidi, C.H. Swanson, G.C. Smith, A. Moschona, S. Hadjispyrou, A. Salifoglou, A.A. Pantazaki, M. Pelecanou, G. Litsardakis, Magnetic cationic liposomal nanocarriers for the efficient drug delivery of a curcumin-based vanadium complex with anticancer potential, J. Inorg. Biochem. 199 (2019) 110778, https://doi.org/10.1016/j.jinorgbio.2019.110778.

[79] M. Prokopowicz, Silica-polyethylene glycol matrix synthesis by sol-gel method and evaluation for diclofenac diethyloammonium release, Drug Deliv. 14 (2007) 129–138, https://doi.org/10.1080/10717540600812653.

[80] G. Berlier, L. Gastaldi, E. Ugazio, I. Miletto, P. Iliade, S. Sapino, Stabilization of quercetin flavonoid in MCM-41 mesoporous silica: positive effect of surface functionalization, J. Colloid Interface Sci. 393 (2013) 109–118, https://doi.org/ 10.1016/j.jcis.2012.10.073.

[81] A. Mehmood, H. Ghafar, S. Yaqoob, U.F. Gohar, B. Ahmad, Mesoporous silica nanoparticles: a review, J. Develop. Drugs 6 (2017) 174–184, https://doi.org/ 10.4172/2329-6631.1000174.

[82] W. Zhao, M. Lang, Y. Li, L. Li, J. Shi, Fabrication of uniform hollow mesoporous silica spheres and ellipsoids of tunable size through a facile hard-templating route, J. Mater. Chem. 19 (2009) 2778–2783, https://doi.org/10.1039/B822444G.

[83] A.R. Salomon, K.J. Marcinowski, R.P. Friedland, M.G. Zagorski, Nicotine inhibits amyloid formation by the beta-peptide, Biochemistry 35 (1996) 13568–13578, https://doi.org/10.1021/bi9617264.

[84] K. Ono, Y. Yoshiike, A. Takashima, K. Hasegawa, H. Naiki, M. Yamada, Potent anti-amyloidogenic and fibril-destabilizing effects of polyphenols in vitro: implications for the prevention and therapeutics of Alzheimer's disease, J. Neurochem. 87 (2003) 172–181, https://doi.org/10.1046/j.1471-4159.2003.01976.x.

[85] K. Jimenez-Aliaga, P. Bermejo-Besc´os, J. Benedí, S. Martín-Arag´on, Quercetin and rutin exhibit antiamyloidogenic and fibril-disaggregating effects in vitro and potent antioxidant activity in APPswe cells, Life Sci. 89 (2011) 939–945, https://doi.org/ 10.1016/j.lfs.2011.09.023.

[86] M. Hirohata, K. Hasegawa, S. Tsutsumi-Yasuhara, Y. Ohhashi, T. Ookoshi, K. Ono, M. Yamada, H. Naiki, The anti-amyloidogenic effect is exerted against Alzheimer's beta-amyloid fibrils in vitro by preferential and reversible binding of flavonoids to the amyloid fibril structure, Biochemistry 46 (2007) 1888–1899, https://doi.org/ 10.1021/bi061540x.

[87] S.H. Omar, Biophenols pharmacology against the amyloidogenic activity in Alzheimer's disease, Biomed. Pharmacother. 89 (2017) 396–413, https://doi.org/ 10.1016/j.biopha.2017.02.051.

[88] Z. Datki, A. Juh´asz, M. G´alfi, K. So´os, R. Papp, D. Z´adori, B. Penke, Method for measuring neurotoxicity of aggregating polypeptides with the MTT assay on differentiated neuroblastoma cells, Brain Res. Bull. 62 (2003) 223–229, https:// doi.org/10.1016/j.brainresbull.2003.09.011.

[89] S. Bastianetto, R. Quirion, Natural extracts as possible protective agents of brain aging, Neurobiol. Aging 23 (2002) 891–897, https://doi.org/10.1016/S0197-4580 (02)00024-6.

[90] M.A. Ansari, H.M. Abdul, G. Joshi, W.O. Opii, D.A. Butterfield, Protective effect of quercetin in primary neurons against Abeta(1-42): relevance to Alzheimer's disease, J. Nutr. Biochem. 20 (2009) 269–275, https://doi.org/10.1016/j. jnutbio.2008.03.002.

[91] N. Lewinski, V. Colvin, R. Drezek, Cytotoxicity of nanoparticles, Small 4 (2008) 26–49, https://doi.org/10.1002/smll.200700595.

[92] C.P. LeBel, H. Ischiropoulos, S.C. Bondy, Evaluation of the probe 2',7'- dichlorofluorescin as an indicator of reactive oxygen species formation and oxidative stress, Chem. Res. Toxicol. 5 (1992) 227–231, https://doi.org/10.1021/ tx00026a012.

[93] S. Varadarajan, S. Yatin, M. Aksenova, D.A. Butterfield, Review: Alzheimer's amyloid beta-peptide-associated free radical oxidative stress and neurotoxicity, J. Struct. Biol. 130 (2000) 184–208, https://doi.org/10.1006/jsbi.2000.4274.

[94] Y. Li, S. Zhou, J. Li, Y. Sun, H. Hasimu, R. Liu, T. Zhang, Quercetin protects human brain microvascular endothelial cells from fibrillar β-amyloid1-40-induced toxicity, Acta Pharm. Sin. B 5 (2015) 47–54, https://doi.org/10.1016/j.apsb.2014.12.003.